Combustion and Flame 257 (2023) 112487

Contents lists available at ScienceDirect

Combustion and Flame

journal homepage: www.elsevier.com/locate/combustflame

Systematically derived thermodynamic properties for alkane oxidation

Sarah N. Elliott[a,*], Kevin B. Moore III[a], Andreas V. Copan[b], Yuri Georgievskii[a], Murat Keçeli[c], Kieran P. Somers[d], Manik K. Ghosh[d], Henry J. Curran[d], Stephen J. Klippenstein[a]

[a] Chemical Sciences and Engineering Division, Argonne National Laboratory, Lemont, IL 60439, USA
[b] Natural Sciences Department, Emmanuel College, Franklin Springs, GA 30639, USA
[c] Computational Science Division, Argonne National Laboratory, Lemont, IL 60439, USA
[d] Combustion Chemistry Centre, School of Biological and Chemical Sciences, Ryan Institute, MaREI, University of Galway, Galway, Ireland

ARTICLE INFO

Article history:
Received 1 July 2022
Revised 24 October 2022
Accepted 28 October 2022
Available online 11 January 2023

Keywords:
Low-temperature oxidation
Thermodynamics
Ab initio
Heat capacity
Entropy
Gibbs energy

ABSTRACT

Key combustion properties, such as ignition delay time, show strong sensitivity to the thermochemistry of the main species in the standard radical oxidation pathway at low temperatures (600–1000 K). Significant uncertainties persist in current estimates of thermodynamic properties, particularly for the larger species of relevance to common practical fuels. In this article, we use advanced computational schemes to evaluate thermodynamic properties for the fuel, fuel radical, peroxy, hydroperoxy-alkyl radical, and hydroperoxide species for a set of 17 fuels containing up to 9 carbon atoms, and with various degrees of branching in the alkane backbone. The procedure, termed **STAR-1D**, combines conformer sampling to find the minimum geometry, B2PLYP-D3/cc-pVTZ harmonic frequency evaluations, and ωB97X-D/cc-pVTZ one-dimensional torsional mapping. It includes two physically-based scaling routines: a frequency-dependent scaling to B2PLYP-D3/cc-pVTZ anharmonic frequencies and a scaling of one-dimensional ωB97X-D/cc-pVTZ torsional profiles to reproduce the product of the B2PLYP-D3/cc-pVTZ frequencies in the harmonic limit. Substantive comparisons with existing experimental databases, together with careful examinations of key theoretical assumptions, are used to explore the accuracy of the predictions. These computationally intensive explorations of 195 species were facilitated by automated thermochemistry software. High accuracy 0 K heats of formation from a separate study are used with the **STAR-1D** computations to generate NASA polynomial representations. In addition to their intrinsic value, the present results also provide a reliable database for the optimization of group additivity or machine learning schemes for scaling to larger combustion systems. Towards this end a complementary extensive conformational analysis is carried out for the medium sized species and the thermodynamic properties of the lowest energy hydrogen-bonded and non-hydrogen bonded conformers are contrasted for larger hydroperoxy-alkyl radical species.

1. Introduction

Quantitative chemical modeling of complex reactive environments (e.g., a combustion chamber or the atmosphere) commonly relies on accurate descriptions of the thermodynamic and transport properties of hundreds to thousands of species as well as the rate constants for the reactions that connect these species [1]. Within combustion, such modeling finds utility in the development of new and improved devices, the consideration of alternative fuels and additives, and the reduction of pollutants. Thermodynamic properties play a central role in combustion modeling through their connection to heat release. More generally, they are important in determining the equilibrium concentrations of various species, and as a result, the kinetic role of various pathways.

Notably, under low temperature combustion conditions (e.g., 600 to 1000 K), simulated ignition delay times are extremely sensitive to the thermodynamic properties of the peroxy, $\mathbf{R\dot{O}_2}$, hydroperoxy-alkyl radical, $\mathbf{\dot{Q}OOH}$, and hydroperoxy-alkylperoxy $\mathbf{\dot{O}_2}$QOOH species because of their impact on calculated equilibrium constants and reverse rate coefficients [2–4]. For example, a recent study of vom Lehn et al. [3] on diethyl ether oxidation indicates uncertainties in the ignition delay of factors of 12, 5, and 3 for uncertainties of 2.75 kcal mol^{-1} in the heats of formation, 2.4 cal mol^{-1} K^{-1} in the entropies, and 10% in the heat capacities, respectively. The latter parameter uncertainties were considered to be representative of those in the underlying model used as a reference. Meanwhile, in a follow up study, vom Lehn et al. [4] found

* Corresponding author.
E-mail address: elliott@anl.gov (S.N. Elliott).

https://doi.org/10.1016/j.combustflame.2022.112487
0010-2180/

that ignition delay group additivity (GA) sensitivity was highest for groups involved in the low-temperature chain-branching pathways – specifically those that represent OO and OOH moieties and their adjacent groups in $\mathbf{R\dot{O}_2}$, $\mathbf{\dot{Q}OOH}$, $\mathbf{\dot{O}_2QOOH}$ radicals.

The thermochemical properties of many fuel molecules have been studied experimentally, although commonly only at relatively low temperatures. In contrast, for the $\mathbf{\dot{Q}OOH}$ radicals, which play a central role in low temperature chain branching, there is no experimental data due to their ephemeral nature, with very few exceptions [5] or even characterizations through indirect kinetic measurements. Meanwhile, for the fuel radicals $\mathbf{\dot{R}}$, as well as a few $\mathbf{R\dot{O}_2}$, and hydroperoxide molecules $\mathbf{RO_2H}$ some limited experimental data exists [6–12]. The lack of experimental data has led to the common use of either empirical methods, such as GA schemes, or ab initio calculations in estimating the properties.

Group additivity methods assign additive contributions, called group additivity values (GAVs), to enthalpies, entropies, and heat capacities, from the atomic and molecular groups that constitute a molecule [13,14]. Inherently, thermochemistry produced with GA methods is contingent on how completely a set of groups represents the exclusive interactions in a molecule. Additionally, because GAVs must be optimized on an established dataset, GA thermochemistry is sensitive to two further considerations: how thoroughly and independently the molecules in the dataset cover the GA groups and how accurate the dataset's thermochemistry is. Historically, these datasets were aggregations of experimental values [13], which are updated in several reviews (see, e.g., Refs. [15–19]). The development of the hydrogen bond increment (HBI) method by Lay et al. [20] provides a simple means for extending the GA scheme to radicals. However, the absence of experimental spectroscopic data for $\mathbf{\dot{Q}OOH}$ species limits the accuracy of an experimentally based HBI GAV scheme for these key combustion intermediates.

Efforts to circumvent experimental limitations, and to achieve greater consistency, have led to the formulation of datasets through ab initio computations performed specifically with GAV optimization in mind. Enormous numbers of theoretical studies have focused on the determination of the 0 and/or 298 K heat of formation for large sets of species. Here, we are instead specifically interested in mapping out the temperature dependence of the partition functions, or correspondingly the entropies and heat capacities needed to generate the thermodynamic properties at combustion relevant temperatures. Ab initio datasets for these thermodynamic parameters are more limited, since they require extra computation to build vibrational and torsional partition functions. Nevertheless, several efforts to build such thermodynamic property datasets have been reported and include calculations based on HF/6-31G* [21–23], B3LYP/6-31G* [24–28], B3LYP/6-311G** [29,30], B3LYP/6-31+G** [31], and B3LYP/6-31+G(2df,p) [32], density functional methods. Burke et al. [33] compiled many such updates to recommend new GAVs, altering molar entropy contributions, per group, by up to 3.5 cal mol^{-1} K^{-1} and heats of formation by up to 2.9 kcal mol^{-1} from previous values. With every instance of an atomic or chemical group in a molecule, its uncertainty propagates, leading to potentially quite large uncertainties for large molecules.

Recent years have delivered an increased affordability and reliability for high accuracy electronic structure calculations. Furthermore, newly developed software packages, such as AutoMech, QTC, Arkane, and EStokTP, greatly facilitate the application of ab initio methods to the determination of thermodynamic properties through automated workflows (see, e.g., Refs. [34–37]). This progress compels an update to combustion modeling parameters that will, in turn, facilitate a deeper understanding of fuel chemistry. Here, as our first substantive application of the AutoMech and QTC codes, we have systematically determined the thermodynamic properties of relevance to the first stage of oxidation of alkane fuels, initiated with a hydrogen abstractor, X (e.g., $\dot{O}H$, $H\dot{O}_2$, $\dot{H}$, O_2, or $\dot{O}$), and propagated.

$$\mathbf{RH + X \rightleftharpoons \dot{R} + HX}$$
$$\mathbf{\dot{R} + O_2 \rightleftharpoons R\dot{O}_2 \rightleftharpoons \dot{Q}OOH}$$
$$\mathbf{RH + R\dot{O}_2 \rightleftharpoons \dot{R} + RO_2H}$$

In particular, we have determined the entropy, enthalpy, heat capacity, and Gibbs energy for the fuel **RH**, the corresponding $\mathbf{\dot{R}}$, $\mathbf{R\dot{O}_2}$, and $\mathbf{\dot{Q}OOH}$ radicals, and the alkylhydroperoxide, $\mathbf{RO_2H}$, molecules for a set of 17 fuels over the temperature range 200–3000 K. This set of fuels ranges from C_1–C_9 species and includes a variety of degrees of branching along the hydrocarbon backbone. The large range of branching patterns and long range interactions included in this set provides broad coverage of the sets of interactions required for the determination of quantitatively meaningful GAVs and effective machine learning. Towards this goal, contemporaneous work [38] takes advantage of the dataset presented here to update and formulate novel GAVs for 298 K heats of formation. Related work to update GAVs for the entropy and the temperature dependent heat capacities is in progress. An extension of this dataset to include the data from a large set of conformational mappings provides further constraints for such GAV optimizations. Of course, this data will also find direct utility in low temperature oxidation simulations.

Prior ab initio thermodynamic studies from the groups of Bozzelli [20,39–45], Vansteenkiste [46–48], Green [22,23,49,50], Dean [28,51], and Miyoshi [52], have targeted many of these species with related theoretical methods. This work builds from these earlier studies and proceeds beyond them in a variety of ways. As with these prior studies, the present work employs a separation of modes into a set of torsional modes and the remaining vibrational modes, which are generally of higher frequency. Furthermore, in the interest of computational expediency, we also treat the torsional modes as effective one-dimensional hindered rotors (1DHR), while the remaining modes are treated within a rigid-rotor harmonic-oscillator (RRHO) framework. However, we work to systematically improve both the 1DHR and RRHO treatment. In particular, our 1DHR treatment includes a simple scaling to reproduce the proper harmonic limit, and a variety of methods are used to improve the consistency of the torsional potentials across regions of hysteresis. Meanwhile, the RRHO treatment includes a frequency dependent scaling relation designed to reproduce a reference set of anharmonic vibrational frequencies. Furthermore, the reference frequencies are now determined from a higher quality doubly hybrid density functional method. Finally, we employ a set of high accuracy CBH-ANL 0 K heats of formation (with $2\sigma = 0.2$–0.5 kcal mol^{-1}) determined in a companion study [53] in the generation of NASA polynomial thermochemical representations appropriate for chemical modeling purposes.

Another key aspect of the present work is a sequence of analyses that explore the validity of various assumptions and the effectiveness of the overall approach. For instance, honing in on the $\mathbf{\dot{Q}OOH}$ species, the differences between calculated partition functions for hydrogen bonded and non-hydrogen bonded configurations provides some indication of the uncertainties arising from multi-dimensional corrections. For several species, we directly contrast scaled 1DHR properties to those obtained with full multi-dimensional partition functions. Meanwhile the torsional mappings are validated by comparing the DFT predicted torsional potential with large basis set coupled cluster torsional potentials.

Within the RRHO + 1DHR framework, partition functions are sensitive to the selection of a reference conformer. At combustion temperatures, the ground electronic conformer often no longer dominates, largely due to the nonsynchronous scaling of enthalpy and entropy with temperature. For species up to seven heavy atoms we carry out a extensive conformational analysis, which ex-

amines the sensitivity of the reference conformer selection to the electronic structure method. Comparison between two configurations for a single species is incredibly useful in choosing and evaluating group additivity parameters. In particular, it helps isolate specific short or long-range interactions. As group additivity aims for increasingly quantitative fits, new groups are identifiable by finding deviations between the ab initio and GA conformer energy ordering. Conformational analysis also presents a means of calculating high-level fitting data with small species that contains unfavorable group interactions that only appear in the ground conformer of large, highly-branched species.

For the alkane series, comparisons to experimentally derived thermodynamic properties are used to evaluate the importance and effectiveness of the new scaling relations, as well as the overall scaled RRHO + 1DHR procedure. Finally, for the $\dot{\mathbf{R}}$ and $\mathbf{R\dot{O}_2}$ radicals, more limited comparisons with experiment help to further validate the overall methodology.

2. Theoretical methodology

We here develop a protocol for **S**ystematic **T**hermochemistry built from **A**NL **R**eference energies and an RRHO + **1D**HR partition function model (**STAR-1D**). Within this protocol, 0 K heats of formation ($\Delta H_f(0\ K)$), which are needed to generate absolute thermochemistry, are obtained from second order connectivity based hierarchical (CBH2) [54–56] calculations. In essence, the CBH2 scheme provides an optimal readily automated isodesmic reaction scheme, which requires reference data for a limited set of molecules continuing up to about five heavy atoms. The reference data used in the CBH2 calculations is high-level ANL0 energies laddered with ANL1 energies [57] in a CBH1 calculation. The $\Delta H_f(0\ K)$ evaluation applies this reference data in a CBH2 equation to CCSD(T)-F12b/cc-pVTZ-F12 and CCSD(T)-F12b/cc-pVDZ-F12 electronic energies paired with scaled B2PLYP-D3/cc-pVTZ zero point vibrational energies (ZPVEs). This CBH-ANL procedure to evaluate $\Delta H_f(0\ K)$ is described in a separate publication [53], where we assign 2σ uncertainties of 0.2–0.5 kcal mol^{-1} to the final $\Delta H_f(0\ K)$ predictions. Meanwhile, the thermodynamic analysis within the **STAR-1D** protocol, which is the focus of this work, employs an RRHO + 1DHR model that is improved with physically motivated scaling procedures, as outlined below. Both production of the thermodynamic properties and computation of the electronic structure properties are carried out with automated workflow codes [34,35].

2.1. Thermodynamic model

The RRHO + 1DHR partition functions (Q), are obtained by calling the partition function code in MESS [58].

$$Q = \frac{1}{\sigma_{\text{eff}}} Q_T Q_R Q_V Q_e \prod_i q_{\text{HR},i} \tag{1}$$

The translational, Q_T, rigid rotational, Q_R, harmonic vibrational, Q_V, and electronic, Q_e, partition functions are determined from the mass, structure, vibrational frequencies, and electronic energy levels determined with the ab initio simulations. The effective symmetry number, σ_{eff}, is specified as the rotational symmetry number divided by the number of enantiomers. At low temperatures, MESS generates the torsional partition function ($q_{\text{HR},i}$) for each torsional mode, i, from the eigenvalues $E_j(\theta)$ of the Schrödinger equation for the corresponding torsional potential, $V(\theta)$:

$$q_{\text{HR},i} = \frac{1}{\sigma_i} \sum_j \exp\left(\frac{-E_j(\theta)}{k_B T}\right) \tag{2}$$

where k_B is Boltzmann's constant and σ_i is the periodicity of the corresponding torsional mode. For higher energy states, the direct sum is converted to a semiclassical integral. The underlying torsional potentials, $V(\theta)$ are represented as Fourier expansions or spline fits of torsional scans, where only the torsional coordinate is constrained. Within the present RRHO + 1DHR treatment, the vibrational frequencies required for the evaluation of Q_V are calculated after automatically projecting the torsional modes from the Hessian with the ProjRot utility of EStoKTP [37].

We select a temperature range of 200–3000 K for the partition function evaluations in order to cover the full range of combustion and atmospheric interests. The subsequent conversion of Q to NASA polynomials is accomplished with PAC99 [59], using 1000 K as the connection between the low and high temperature coefficients. The final output of the data is in ChemKin format as well as CSV files of thermochemical properties. During the process of building the MESS input, the code processes several novel scalings of the electronic structure properties, as described in later sections. Section 2.2 describes the automation of the process.

2.2. Automation of electronic structure properties

Within the **STAR-1D** protocol, hundreds of ab initio computations are required for each of the larger species. This work automates the computations through a combination of the Quantum Thermochemistry (QTC) [34] and AutoMech [35] software suites. The QTC package was used in early stages of this project. The AutoMech package can be considered as the successor to QTC. It provides some advanced features that proved useful for the later stages of this effort. All aspects of the **STAR-1D** protocol are directly implemented in AutoMech, including a preliminary conformational sampling, conformer selection, torsional mapping, harmonic and anharmonic frequency evaluations, high level electronic energy determination, CBH reference reaction correction, an on-the-fly implementation of the scaling procedures, partition function determination, and NASA polynomial generation. This automation includes data production and collection for the full set of routines and applications, thereby greatly facilitating the development and application of the present **STAR-1D** protocol.

In a companion work [53], we used the QTC software to compute reliable $\Delta H_f(0\ K)$ values for our full set of 195 alkane oxidation species. In doing so, we developed a database of electronic structure properties for our target species. After a geometry optimization module, this database houses properties in a location determined by a species specifier and a theory specifier. All subsequent QTC modules use this geometry as their input geometry, and nest the auxiliary properties (i.e., single point energy or frequencies) under it with an additional theory specifier. From this QTC database, and new calls to the QTC electronic structure drivers, we collect the electronic structure parameters that build up Eqs. (1) and (2).

The **STAR-1D** protocol, as such, begins with an ωB97X-D/6-31G* [60] conformational sampling, for the lesser of 100 and $6 + 2 \times 3^N$ samples, where N is the number of non-methyl torsional angles. The ωB97X-D functional is a well-motivated range-separated functional that includes empirical dispersion corrections. The underlying frequencies and geometries are obtained with the double-hybrid method B2PLYP-D3/cc-pVTZ [61,62], which provides CCSD(T) quality geometries and frequencies at a small fraction of the cost. For the CBH-ANL high-level energies we use CCSD(T)-F12b/cc-pVTZ-F12 [63] single point energies for species with eight heavy atoms or fewer, and CCSD(T)-F12b/cc-pVDZ-F12 energies for the larger species. To calculate $V(\theta)$ for $q_{\text{HR},i}$, we use the QTC driver to carry out one-dimensional scans along each of the torsional angles in 30° increments. Each scan point geometry is built from the previous one and is optimized at ωB97X-D/cc-pVTZ [60,62] after updating and freezing the dihedral angle of the scan.

The suitability of this cost-effective functional for the 1DHR analyses is evaluated in Section 3.3.

2.3. Reference conformer selection

The **STAR-1D** protocol relies on the determination of a reference conformer from which the RRHO and 1DHR analyses are performed. This reference conformer is traditionally taken to be the conformer of lowest electronic energy, as determined through grid based sampling of expected conformational minimum. We instead apply a Monte Carlo sampling based approach, where each of the torsional degrees of freedom is randomly sampled within its range, and a full optimization is then performed. This process is then repeated until a preset number of optimizations have been performed, which was the minimum of 100 and $6+2(3^n)$ where n is the number of non-methyl torsional coordinates. This approach removes the bias of presuming a starting grid of conformational geometries and is effective at finding a nearly global minimum with a relatively modest number of samplings. We find it is particularly effective in considering molecules with large numbers of torsional degrees of freedom. However, it is not guaranteed to find the lowest conformer. The QTC code selects the reference conformer as the structure with the lowest electronic energy from the full set of ωB97X-D/6-31G* [60,64] geometry optimizations. The work done in QTC, therefore, relied on three assumptions:

1. the number of sampling points was sufficient to find the global minimum on the ωB97X-D/6-31G* PES,
2. the ωB97X-D/6-31G* PES is reasonably similar to a PES that would be achieved from higher levels of theory, and
3. the zero-point vibrational energy will not significantly alter the conformer ordering.

In applying the QTC database to evaluate thermochemical properties we add a fourth assumption:

4. the minimum energy conformer at 0 K will be the dominant conformer at combustion temperatures.

As noted above, QTC can store only one geometrical configuration per level of theory, which to some degree limits the types of conformational analyses that can be performed. In contrast, the newly developed AutoMech software suite [35] is able to store, and perform auxiliary computations on all local energetic minimum structures for a level of theory. AutoMech, thereby, enables us to evaluate the validity of these assumptions through more detailed conformer analyses, see Section 3.1.

2.4. Scaling of vibrational frequencies

Evaluating the vibrational partition function for a species is fundamental to computing its thermochemical properties. At high T, each frequency, and thereby each percent error in frequency, contributes multiplicatively to the vibrational partition function. Moreover, a study by Jasper et al. found that at 2500 K anharmonic corrections for each vibrational mode increased the partition function by 3% on average [65]. Even for a species with as few modes as methane, this would cause a 1 kcal mol^{-1} shift in the Gibbs free energy at 2500 K.

In previous work [66], B2PLYP-D3/cc-pVTZ anharmonic frequencies had an error of 0.31 ± 0.87% from 455 CCSD(T)/CBS anharmonic frequencies calculated for a set of species containing C, N, O, and H and 22 or fewer electrons and we recommend it for medium sized systems. The anharmonic analysis for both of these was carried out with second order vibrational perturbation theory (VPT2) [67]. The success of the B2PLYP-D3/cc-pVTZ approach motivates us to obtain 562 VPT2 B2PLYP-D3/cc-pVTZ anharmonic frequencies for a set of C, H, and O containing species of relevance to hydrocarbon oxidation. The largest of these is ethyl hydroperoxide. We use these calculations to develop a frequency-dependent scaling factor between harmonic (ω) and anharmonic (ν) B2PLYP-D3/cc-pVTZ frequencies. This scaling factor is chosen to minimize the error in the ratio between harmonic and anharmonic frequencies ($\frac{\omega}{\nu}$), rather than the absolute error of frequencies. This, in effect, directly minimizes the error in the resulting partition functions.

We represent the frequency dependence of the scaling factor as $s(\omega) = a - b * \omega^c$. The optimization results in: $a = 1.045$, $b = 0.00851$, and $c = 0.292$. Figure 1(a) shows the ratio ($\frac{\omega}{\nu}$) along with the optimized equation for $s(\omega)$. The resulting scaled harmonic frequencies are displayed in Fig. 1(b). The mean absolute error in scaled frequencies, $|\omega_s - \nu|$, where $\omega_s = s(\omega) * \omega$, is 7.4 cm^{-1} and its RMSD is 12.7 cm^{-1}. The mean absolute error of the ratio, $\frac{|\omega_s - \nu|}{\nu}$, is 0.45% with an RSMD of 0.69% and a $2\sigma(\omega_s) = 1.4$%. The full set of data for this analysis and details of the optimization are given in Section S1 and Table S1.1 of the Supplementary material.

The RRHO + 1DHR vibrational partition function evaluations employ projected harmonic frequencies, $\tilde{\omega}$, where translational, rotational, and torsional modes are projected out of the Hessian. The frequency scaling factor is applied to these projected frequencies to obtain $\tilde{\omega}_s = s(\tilde{\omega}) * \tilde{\omega}$ and the energy level spacings are $\tilde{\omega}_s$. Note, anharmonicity has a nontrivial effect on 0 K heats of formation through a reduced E_{ZPVE}. Explored in a contemporaneous study [53], we apply a direct scaling factor of 0.9864 to the harmonic B2PLYP-D3/cc-pVTZ E_{ZPVE} rather than consider contributions of $\tilde{\omega}_s$.

The uncertainty in a partition function due to the scaled frequency uncertainty is $2\sigma_s(Q)$, and, to illustrate assuming uncorrelated errors, can be calculated with a simple multiplicative uncertainty propagation, $\frac{\Delta z}{z} = \sqrt{\sum_i^{N_v} \left(\frac{\Delta x_i}{x_i}\right)^2}$. Here, $\frac{\Delta z}{z}$ is $2\sigma_s(Q)$ expressed as a percentage, the summation is over the number of frequencies (N_v) after rotational, translational, and torsional projection, and $\frac{\Delta x_i}{x_i}$ is $2\sigma(\omega_s) = 1.4$%. Accordingly, $2\sigma_s(Q) = 0.014\sqrt{N_v}$. The largest species in the fit, ethyl hydroperoxide, has $N_v = 33$ and so has an expected $2\sigma_s(Q) = 8$%. In the larger set of target molecules of this work, we have N_v as large as 69, which would produce $2\sigma_s(Q) = 11$%.

The suitability of this estimation of $2\sigma_{\omega_s}(Q)$ is showcased in Fig. 2. This data shows, for each of the 32 species in the VPT2 dataset, the ratio of its product of scaled frequencies to the product of fundamental frequencies, $\prod_i^{N_v} \omega_{s,i} / \prod_i^{N_v} \nu_i$. From this we see the scaled frequencies produce an mean absolute overall frequency product error for each species of 2.3%, and an RMSD = 4.5%, which is a direct error in the partition function. The greatest error factor is for ethane, which has a scaled frequency product equal to 92% of its the fundamental frequency product and is the only point significantly outside the $2\sigma_s(Q)$ predicted uncertainties for this set.

2.5. Scaling of torsional profiles

We used MESS [58] to perform a Fourier fit on each ωB97X-D/cc-pVTZ torsional profile, $V(\theta)$ and solve the one dimensional harmonic oscillator, see Eq. (2). When driven by AutoMech, MESS additionally performs a precursory spline fit. The resulting harmonic oscillator frequency, Ω_j, corresponds to that for the jth torsional mode. Under the assumption that the torsional vibrational modes are fully uncoupled, Ω_j should be consistent with the vibrational frequency ω_j that is calculated from the B2PLYP-D3/cc-pVTZ harmonic frequency analysis, which was performed in Gaussian09. These frequencies would differ only due to their differing levels of theory. In this case, we could approximate a B2PLYP-D3/cc-pVTZ torsional profile by scaling the energies along the ωB97X-D/cc-pVTZ torsional profile, $V(\theta)$, to enforce $\Omega_j = \omega_j$. Coupling is present between the vibrational modes, however, so we instead perform this scaling over the full vibrational spectrum. By doing

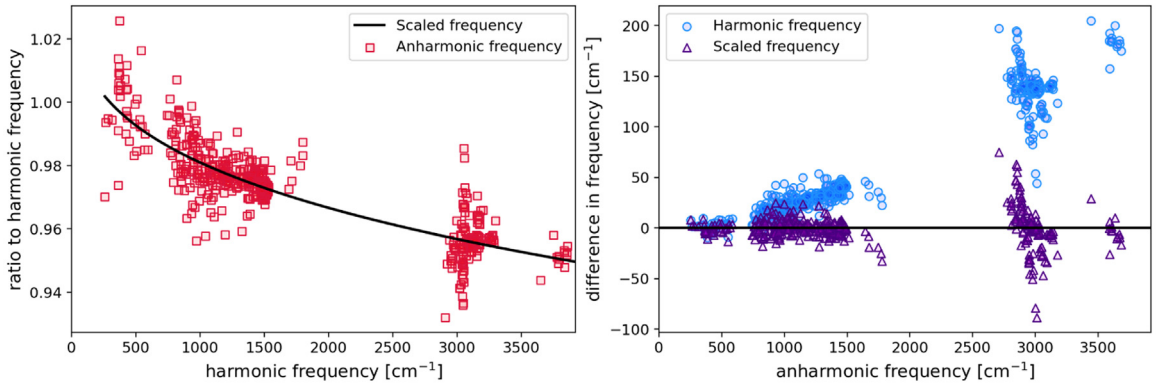

(a) The red squares represent each ratio, ν/ω, plotted against ω. The black line is s(ω).

(b) The blue circles represent ω-ν plotted against ω. The purple triangles are ω_s-ν.

Fig. 1. B2PLYP-D3/cc-pVTZ VPT2 anharmonic frequencies (ν) compared to B2PLYP-D3/cc-pVTZ harmonic frequencies (ω) and scaled B2PLYP-D3/cc-pVTZ harmonic frequencies (ω_s) for 562 frequencies. The ω_s = s(ω)ω, where s(ω) = a - b $\times\omega^c$. The parameters a, b, and c were optimized with these 562 frequencies to be $a = 1.045$, $b = 0.00851$, and $c = 0.292$.

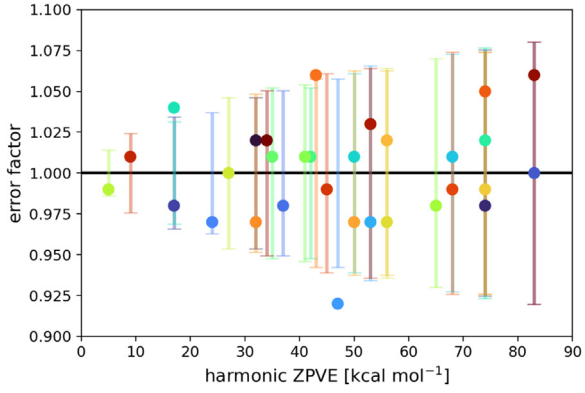

Fig. 2. The error contribution of scaled frequencies (ω_s) to the partition function for each of the 32 species that are used in the frequency scale factor fit plotted against their harmonic ZPVE. This error factor, compared to a partition function built from the VPT2 fundamental frequencies (ν), is $\prod_i^{N_\nu} \omega_{s,i} / \prod_i^{N_\nu} \nu_i$, where N_ν is the number of vibrational frequencies for each species. The bars show the estimated propagated uncertainty for each species based on a $2\sigma(\omega_s) = 1.4\%$ for each of its modes.

so, we account for contributions of off-diagonal terms to Ω_j that are otherwise neglected when solving the HO for a single torsional profile. The expression for the scaling factor, s_V, that is applied to each torsional profile is shown in Eq. (3).

$$s_V = \left(\frac{\prod_{i=1}^{N_\nu} \omega_i}{\left(\prod_{i=1}^{N_\nu - N_t} \tilde{\omega}_i\right)\left(\prod_{j=1}^{N_t} \Omega_j\right)} \right)^{\frac{2}{N_t}} \tag{3}$$

Here, N_ν is the number of vibrational modes, N_t is the number of torsions, ω_i is the ith B2PLYP-D3/cc-pVTZ harmonic vibrational frequency, $\tilde{\omega}_i$ is the ith projected B2PLYP-D3/cc-pVTZ harmonic vibrational frequency, and Ω_j is the jth harmonic frequency corresponding to the jth ωB97X-D/cc-pVTZ torsional profile, and the expression is squared due to the quadratic scaling of a potential with respect to its harmonic oscillator frequency.

It is challenging to obtain accurate values of density functional based harmonic frequencies for extremely low-frequency motions due to issues with the accuracy of grid based integrations. Furthermore, for such low-frequency modes, B2PLYP-D3/cc-pVTZ itself is not necessarily particularly accurate. The net result is that such modes lead to unreliable scaling factor predictions. Furthermore, for such low frequency modes, the torsional barriers tend to be quite low, and the partition functions are then not very sensitive to the torsional profile. As a result, modes with frequency less than 20 cm^{-1} are identified and excluded in the process of determining a scale factor. The corresponding modes do not undergo any scaling. In Section 3.5 we discuss problems that arise with Eq. (3) with umbrella motions.

2.6. Hysteresis in torsional profiles

During the torsional scan routine, AutoMech or QTC update a torsional angle by the given step size (15° and 30°, respectively) and perform the ωB97X-D/cc-pVTZ geometry optimization. The resulting geometry is used as the starting geometry for the next step. Because the optimizations are local, building from the optimal geometry for the previous scanning dihedral angle, the routine can become trapped in configurations that are not the lowest energy for that frozen dihedral angle. When present, this hysteresis is often most apparent between the initial and final geometry along a scan. As a result, the hysteresis produces a non-harmonic profile around the minimum. QTC relies on EStokTP, and larger step sizes, to avoid hysteresis. AutoMech identifies potential points of hysteresis by subtracting an Akima spline fit [68,69] from a periodic spline fit. If they vary at any point by a threshold, the code will then run a backward scan until it resolves that hysteresis. Away from the end point minima this procedure is not always effective, but away from the minima such hystereses are less problematic for the present analysis.

The scans also occasionally suffer from negative potentials. They occur for two reasons. First, the ωB97X-D/cc-pVTZ scans are performed about a reference conformer that was the minimum on the ωB97X-D/6-31G* PES. If the global minimum structure on the ωB97X-D/cc-pVTZ PES differs from that on the ωB97x-D/6-31G* PES, and is captured during the ωB97X-D/cc-pVTZ scan, the profile will have a relative negative energy. QTC resolves this by restarting the **STAR-1D** workflow with the ωB97x-D/cc-pVTZ minimum as the selected conformer. AutoMech, simply replaces the negative potential value with zero (although one can also choose to reoptimize the geometry as with QTC). We find a similar issue for 31 **ȮOOH** species, because we choose to start with the lowest energy non-hydrogen bonded (nHB) structure rather than the global minimum. The scan may walk into lower energy hydrogen bonded (HB) configurations. AutoMech again replaces the negative potential with zero. QTC can only perform auxiliary com-

Table 1
The difference (δ) in energy (in kcal mol^{-1}) between the reference conformer and the lowest energy conformer.[a].

Species	SMILES	δE_{elec}				δZPVE	δH
		L1[b]	L2[c]	L3[d]	L4[e]	L2	L5[f]
$CH_3CH(CH(CH_3)CH_3)CH_3$	CC(C(C)C)C	0.20	0.00	−0.10	−0.10	−0.03	−0.14
$CH_3CH_2CH_2\dot{C}H_2$	CCC[CH2]	0.00	−0.18	−0.23	−0.22	−0.09	−0.32
$CH_3CH_2\dot{C}HCH_2CH_3$	CC[CH]CC	−0.13	−0.34	−0.34	−0.34	−0.23	−0.57
$CH_3CH_2CH_2CH_2\dot{C}H_2$	CCCC[CH2]	0.23	−0.13	−0.19	−0.18	−0.09	−0.28
$CH_3\dot{C}HCH_2CH_2CH_3$	C[CH]CCC	0.07	−0.12	−0.20	−0.20	−0.13	−0.32
$CH_3CH_2\dot{C}HCH_2CH_2CH_3$	CC[CH]CCC	0.13	−0.08	−0.18	−0.17	−0.14	−0.31
CH_3CH_2OOH	CCOO	0.39	−0.05	−0.22	−0.22	−0.06	−0.28
$(CH_3)_2CHOOH$	OOC(C)C	0.19	0.01	−0.11	−0.11	−0.03	−0.13
$CH_3CH_2CH_2OOH$	CCCOO	0.10	−0.15	−0.27	−0.27	−0.01	−0.27
$(CH_3)_2CHCH_2OOH$	OOCC(C)C	0.10	−0.16	−0.30	−0.29	−0.02	−0.31
$CH_3CH_2CH_2CH_2OOH$	CCCCOO	0.12	−0.15	−0.29	−0.28	0.00	−0.28
$(CH_3)_2\dot{C}CH_2OOH$	OOC[C](C)C	0.13	−0.11	−0.30	−0.29	0.08	−0.21
$CH_3CH(OOH)CH_3\dot{C}H_2$	CC(OO)C[CH2]	0.43	−0.35	−0.61	−0.58	−0.23	−0.82
$CH_3CH(OOH)\dot{C}HCH_3$	CC(OO)[CH]C	0.13	−0.32	−0.22	−0.18	−0.11	−0.29
$CH_3CH(\dot{C}H_2)CH_2OOH$	OOCC([CH2])C	0.40	−0.55	−0.89	−0.85	−0.31	−1.16
$CH_3CH(OOH)CH_2\dot{C}H_2$	[CH2]C(OO)CC	0.21	−0.11	−0.13	−0.13	0.02	−0.11
$\dot{C}H_2CH_2CH_2CH_3OOH$	[CH2]CCCOO	0.83	−0.07	−0.28	−0.23	−0.35	−0.58
$CH_3CH_2\dot{C}HCH_2OOH$	CC[CH]COO	1.05	0.32	−0.15	−0.12	−0.42	−0.54
$CH_3\dot{C}HCH_2CH_2OOH$	C[CH]CCOO	0.32	0.01	−0.01	0.00	−0.33	−0.33

[a] For any conformers found during the AutoMech conformer analysis that had a δH(L5) < −0.10 kcal mol^{-1} .
[b] L1: ωB97X-D/6-31G* .
[c] L2: B2PLYP-D3/cc-pVTZ.
[d] L3: CCSD(T)-F12b/cc-pVDZ-F12//B2PLYP-D3/cc-pVTZ.
[e] L4: CCSD(T)-F12b/cc-pVTZ-F12//B2PLYP-D3/cc-pVTZ.
[f] $\delta H(L5) = \delta E_{elec}(L4) + \delta E_{ZPVE}(L2)$.

putations on the minimum conformer and so avoids this pitfall, but by the same token cannot employ nHB structures as reference conformers.

3. Results and discussion

3.1. Conformer selection

In this work we carefully consider the conformer energy ordering. We have carried out a conformer analysis in AutoMech on the subset of species with seven or fewer heavy atoms. This species subset is comprised of 14 alkanes (**RH**), 24 alkyl radicals (**Ṙ**), 8 alkyl hydroperoxide species (**RO$_2$H**), 8 alkylperoxy radicals (**RȮ$_2$**), and 13 hydroperoxy-alkyl radicals (**ȮOOH**) molecules for a total of 67 molecules and 461 conformers. The AutoMech conformer analysis begins by fully repeating the **STAR-1D** ωB97X-D/6-31G* random conformer sampling. Next, it carries out the B2PLYP-D3/cc-pVTZ geometry optimization on all symmetrically unique rotamers that are within 5 kcal mol^{-1} of the global minimum electronic energy structure on the ωB97X-D/6-31G* surface. For each of the resulting rotamer B2PLYP-D3/cc-pVTZ geometries, AutoMech then performs a B2PLYP-D3/cc-pVTZ harmonic analysis and CCSD(T)-F12b/cc-pVXZ-F12 single point energy computations, [X = D,T]. The intent of the analysis is to evaluate the four conformer related assumptions made in the **STAR-1D** protocol, as listed in Section 2.3, and to provide additional data for machine learning and/or GA analyses.

For each species, the **STAR-1D** reference conformer is defined as the lowest ωB97X-D/6-31G* electronic energy found by QTC. To evaluate Assumptions 1, 2, and 3 we have compiled Table S2.2, which shows, for each species, the energies of each rotamer relative to those of the reference conformer (δE_{elec}) for the following levels of theory:

L1: ωB97X-D/6-31G*,
L2: B2PLYP-D3/cc-pVTZ,
L3: F12b-CCSD(T)/cc-pVDZ-F12//B2PLYP-D3/cc-pVTZ, and
L4: F12b-CCSD(T)/cc-pVTZ-F12//B2PLYP-D3/cc-pVTZ.

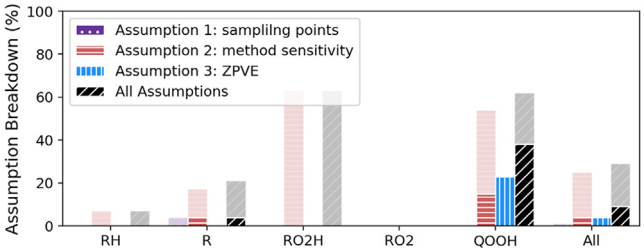

Fig. 3. The percentage of cases where a full **STAR-1D** analysis found conformers lower in energy than the reference conformer. The translucent and opaque bars represent the energy differences that are greater than 0.1 and 0.33 kcal mol^{-1}, respectively. Those that failed due to Assumption 1 (that the number of sampling points is sufficient) are in dotted purple, Assumption 2 (that the conformer ordering is evaluated at a sufficiently high level of theory) are in horizontally-striped red, Assumption 3 (that the ZPVE does not reorder the conformers) are in vertically-striped blue, and any failures in diagonally-striped black. These are broken down into the percent failures for 14 alkane (**RH**), 24 alkyl radical (**Ṙ**), 8 hydroperoxy (**RO$_2$H**), 8 peroxy radical (**RȮ$_2$**), and 13 hydroperoxyalkyl radical (**ȮOOH**) molecules, as well as the combined set of 67 species.

The seventh column shows the relative L2 zero-point vibrational energy, $\delta E_{ZPVE}(L2)$, and the final column shows the relative $\delta H(L5) = \delta E_{elec}(L4) + \delta E_{ZPVE}(L2)$. Table 1 displays this information for the lowest δH(L5) conformer for any species with $\delta H(L5) < -0.1$ kcal mol^{-1} conformers. Depicted with the black bars in Fig. 3, this suggests our combined assumptions lead to reference conformers that are no longer the lowest energy conformer with the higher-level considerations for 1 out of the 14 alkanes, 5 out of the 24 alkyl radicals, 5 out of the 8 hydroperoxides, and 8 out of 13 hyroperoxy-alkyl radicals. If we only consider cases where the conformer differed by more than 0.33 kcal mol^{-1}, the center of our uncertainty range for ΔH_f(0 K), our failures diminish to 1 alkyl radical and 5 hydroperoxyalkyl radical species, which is 9% of the species considered in this analysis.

3.1.1. Assumption 1: number of points

The number of starting geometries that the **STAR-1D** procedure samples is the minimum of 100 and $6 + 2(3^n)$ where n is

the number of non-methyl torsional coordinates. Higher *n*-alkanes have more conformers than would be expected by a 3^n approach based on *trans* and *gauche* positions of torsions, and *a priori* enumeration requires a precise set of sequencing rules [70–73]. Moreover, an excess of samples is a safeguard for the duplication of conformers that occurs with random sampling. Taking a closer look at the cases in Table 1, we find that Assumption 1 fails for only one species, $CH_3CH_2\dot{C}HCH_2CH_3$. Here, the independent Monte Carlo sampling in AutoMech found a lower energy L1 conformer than the one performed in QTC, but this rotamer is only 0.13 kcal mol^{-1} lower. Reversedly, in looking at all of Table S2.2, the sampling in AutoMech did not find the lowest energy conformer that QTC had found in just one additional case. From this, we conclude that our original QTC conformer sampling has a sufficient number of points.

3.1.2. Assumption 2: method sensitivity

In contrast, 79% of the lower energy conformers listed in Table 1 are elucidated as lower energy than the reference conformer during the L2 geometry optimization, and remain so for L3 and L4. This weakens Assumption 2, that the L1 PES is representative of the L2 surface. In fact, 25% of the 67 species set had lower L2, L3, or L4 energy conformers. This can be seen as the red bar in Fig. 3. Assuming an uncertainty of 0.33 kcal mol^{-1}, this percent is reduced to 4%. Even so, we consider Assumption 2 as our greatest source of error, and provide a future recommendation that any L1 conformers within 0.33 kcal mol^{-1} of the electronic minimum should be included in higher-level geometry optimization.

One promising finding from Table S2.2 is that in all but four cases the lowest electronic energy L2 conformer is the lowest electronic energy L4 conformer. For each of these exceptions, the L2 energy difference between the conformer that had the lowest L4 energy and the lowest energy L2 conformer is within 0.04 kcal mol^{-1}. This indicates that the L2 surface is an excellent representation of the coupled-cluster PES. The success of dispersion corrected, double-hybrid functionals for conformer ordering has also been reported by Gruzman et al. and Montgomery and coworkers [73,74]. The ωB97X-D/6-31G* conformer ordering performs similarly to the M06/cc-pVTZ method for *n*-butane, *n*−pentane, and *n*-hexane [73]. Higher order effects, such as those from Diagonal Born Oppenheimer Corrections and scalar-relativistic contributions, have been shown to have negligible effects on relative conformer energies for *n*-pentane [75]. A higher-order correlation contribution, ΔT(Q), did not upset the conformer ordering of *n*-pentane.

3.1.3. Assumption 3: ZPVE contribution

Table S2.2 also gives insight into Assumption 3, that the ZPVE will not significantly alter the conformer ordering. This assumption breaks down in only two cases, omitting species that have a lower energy conformer than the reference already at the B2PLYP-D3/cc-pVTZ level. For $CH_3CH_2\dot{C}HCH_2OOH$ (SMILES: CC[CH]COO), rotamer no. 2 has the lowest L4 electronic energy. The electronic energy for rotamer no. 13 is 0.14 kcal mol^{-1} higher, but its 0.45 kcal mol^{-1} lower ZPVE makes it the lowest H(L5) rotamer. The second case is similar. For $CH_3\dot{C}HCH_2CH_2OOH$ (SMILES: C[CH]CCO), rotamer no. 4 has an L4 electronic energy that is lower by 0.10 kcal mol^{-1} than that of rotamer no. 7, but has a 0.23 kcal mol^{-1} higher ZPVE. Note that none of these rotamers are the reference conformer that the energies in Table 1 are calculated relative to. For both of these species, the lowest electronic energy rotamer has an interaction between the terminal methyl group and the central oxygen of the peroxy group. Compared to this configuration, the ZPVE is much lower in the rotamers with a fully *trans* carbon backbone, where the vibrational motions are not sterically constrained. Visualizations for the rotamers discussed in this section are provided in Figures S2.2(a-d). Note that Assumption 3 did exacerbate already present misordering in several instances.

3.1.4. Assumption 4: temperature dependence

The failure cases for Assumptions 1–3 are largely made up of **ȮOOH** radicals. In fact, apart from the **ȮOOH** subset, the conformer analysis only found conformers with δH(L5) < -0.33 kcal mol^{-1} for 1 of 54 species. The four **ȮOOH** radicals that have δH(L5) < -0.4 kcal mol^{-1}, in Table 1, share a commonality – there is a hydrogen bond (HB) between the carbon radical and the hydrogen of the hydroperoxy group. The 6-31G* basis set is known to overestimate the stabilization energy of hydrogen bonds [76], similar to other small basis sets [77]. Already causing large discrepancies at 0 K, these HBs will increasingly shift the conformer ordering at combustion temperatures. The rigidity of a HB increases the frequencies, which aside, is why the E_{ZPVE}(L2) significantly reorders the conformers for a couple of the **ȮOOH** radicals. The increased frequencies, moreover, lower the partition function and the entropy of a radical. The diminished entropy will increase the Gibbs energy, lowering the weight of the conformer's contribution. For this reason, the **ȮOOH** radicals are the most likely to fail Assumption 4, which is that the minimum energy conformer at 0 K will be the dominant conformer at combustion temperatures.

The relative weight, w_i for the contribution of a conformer, *i*, to the overall partition function of the species with *N* conformers in a fully separable RRHO framework is

$$w_i(T) = \frac{\exp\left(\frac{-\delta H_i}{RT}\right) Q_i(T)}{\sum_j^N \exp\left(\frac{-\delta H_j}{RT}\right) Q_j(T)} \tag{4}$$

where $\delta H_i = \Delta H_i(0\ K) - \Delta H_1(0\ K)$, where ΔH_i is the **STAR-1D** heat of formation of rotamer no. *i* and ΔH_1 is for the reference configuration. Figure 4 shows this weighting for an example **RȮ$_2$** radical (SMILES, CC(O[O])CC) on the left, and **ȮOOH** radical (SMILES, OOC([CH$_2$])C) in the middle. The weight of the reference configuration partition function is dominant for both species at low temperatures. For CC(O[O])CC, even with $\delta H_7 = 0.55$ kcal mol^{-1}, by 1000 K rotamer no. 7 has an equal weight to the reference conformer. A similar effect is seen in the OOC([CH$_2$])C **ȮOOH** radical, which does not form a HB. Partition functions with similar weights will be of similar actual value. For these species, then, the $i > 1$ rotamers will not have a large impact on a Boltzmann weighted partition function.

The effect is completely different for those species from Table 1 that have a HB reference configuration. For these, the weights of the reference conformer are no longer competitive even at room temperature. Figure 4 (right) shows the partition function weighting for OOCC([CH$_2$])C, which has one more CH_2 group than the **ȮOOH** in the center panel making it large enough to fold into a HB structure. Even at 298 K, the reference conformer hardly contributes. Instead, a reasonable replacement for the reference conformer is the L1 lowest energy nHB conformer, shown as the black dashed line. We note that while in all cases, the lowest energy nHB conformer is a significant improvement over the HB conformer for the large **ȮOOH** species, in many cases it is not consistently the highest weighted. While the RRHO model partition functions are highly sensitive to conformer choice, the 1DHR model is less sensitive because other minima are sampled during the torsional scans. Because of this, we consider it sufficient to have chosen a nHB reference conformer that is amongst the top half of RRHO contributors.

3.2. Hydrogen bonding in larger species

For **ȮOOH** species we find through the conformer analysis that Assumptions 1–4 are often invalid. This is because the ground state

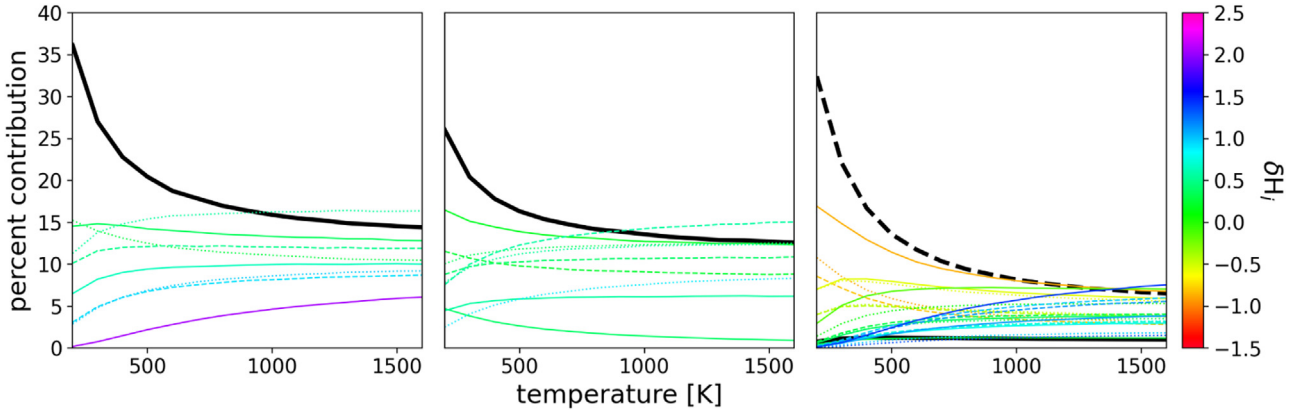

Fig. 4. Percent contribution for each conformer of (left) CC(O[O])CC, (middle) OOC([CH_2])C, and (right) OOCC([CH_2])C for RRHO partition functions. Weights are calculated according to Eq. (4), where the partition function Q is computed with B2PLYP-D3/cc-pVTZ geometries and frequencies and δH_i is the total energy difference between rotamer no. i and the reference conformer at CCSD(T)-F12b/cc-pVTZ-F12 with a scaled ZPVE. The black solid line represents the weight of the reference conformer, the lowest ωB97X-D/6-31G* electronic energy conformer. The black dashed line represents the lowest ωB97X-D/6-31G* energy non-hydrogen bonded conformer.

structure frequently has a hydrogen bond between the radical and the hydrogen atom on the peroxy group. The added rigidity of the structure due to the hydrogen bond increases the frequencies, and thereby diminishes the entropy of the molecule. At combustion temperatures, the Gibbs energy is often affected so significantly that the hydrogen-bonded conformer is not the dominant structure. Such sensitivity was also noted by Green and co-workers, who refer to the hydrogen bonded (HB) structures as ring and the non-hydrogen bonded (nHB) as open structures [50]. This motivated us to add the optional criteria to AutoMech to update the reference configuration to a nHB structure in nHB-**STAR-1D**.

Accordingly, we performed an additional geometry analysis of all 195 species to identify strong hydrogen bonds to the radical carbon or oxygen or to an oxygen lone pair. Using a structural definition, we assume a significant orbital overlap for any species with a C–H···O, C–H···Ċ, or O–H···Ċ distance of 2.43 Å or less and angles of 110° or more. For the 31 species that are thereby categorized as HB structures, which are all **ȮOOH** radicals, we carry out a nHB-**STAR-1D analysis**, which differs from the original only by constraining the evaluation to the lowest energy nHB conformer.

Figure 5 demonstrates the difference in thermochemical properties between the lowest energy HB and nHB conformer for $\dot{C}H_2CH_2CH_2CH_2OOH$. The HB in this species is relatively strong, with a Ċ···H length of 2.27 Å and ∠Ċ···H–O = 156°. At low temperatures, the entropy of the nHB conformer is 15 cal mol^{-1} K^{-1} higher than the HB. At high temperatures, the entropies converge, but the enthalpy of the nHB conformer is more than 10 kcal mol^{-1} lower. This behavior results in a Gibbs energy that is consistently lower for the nHB structure.

Table 2 shows the difference between Gibbs energies for the complete set of nHB and HB structures. The average nHB structure produces a ΔG(1000 K) that is 4.4 kcal mol^{-1} lower than its HB counterpart. Moreover, these HB conformers are all **ȮOOH** species. A constant shift in the **RȮ$_2$** ⇌ **ȮOOH** equilibrium constant of this magnitude dramatically increases fuel reactivity. All final thermochemistry reported in this work, therefore, corresponds to the nHB configurations.

3.3. QM method for torsional profiles

A one-dimensional, hindered rotor (1DHR) treatment of a partition function necessitates that a V(θ) be built from a torsional scan for each hindered rotor (See Eqs. (1) and (2)). Within the **STAR-1D** protocol we constrain only the torsional angle in these scans. For the purposes of testing, we here evaluate torsional profiles computed with M1: ωB97X-D/cc-pVTZ M2: B2PLYP-D3/cc-pVTZ, and M3: CCSD(T)-F12/cc-pVTZ-F12//B2PLYP-D3/cc-pVTZ methods for propane oxidation through the *n*-propyl radical. This includes propane, *n*-propyl radical, *n*-propyl peroxy radical, *n*-propyl hydroperoxide, and *n*-propyl hydroperoxyalkyl radical. Respectively, these species have 2, 2, 3, 4, and 4 torsions (see Figure S3.3). The electronic energy at each scan point is relative to the energy of the reference configuration, allowing for tremendous error cancellation. The M1 torsional scans are employed in the **STAR-1D** V(θ) evaluations.

The *n*-propyl hydroperoxy radical showed the greatest sensitivity to electronic structure method. For it, the shifts in the torsional profiles, ΔV(θ), from M3 are shown on the top panel of Fig. 6. The V(θ) for each method are largely the same shape, but have maximum shift $V(\theta)_{M1-M3}$ of 0.15, 0.50, 0.47, and 0.69 kcal mol^{-1}, which are 22, 15, 8, and 11% of each M3 profile height, $V_{M3,max}$, respectively. The largest maximum shift is in the fourth torsion, which is the ∠C–O–O–H, and the greatest relative shift is the first, which is ∠H–Ċ–C–C. Differences in thermochemical properties, shown in the bottom panel of Fig. 6, elucidate the impact of ΔV(θ). In the combustion relevant 600–1500 K temperature range, highlighted in teal on the figure, the M1 heat capacities and entropies vary by a maximum of 0.26 and 0.12 cal mol^{-1} K^{-1}, respectively, from those of the M3 method. Interestingly, $\Delta C_{M1-M3}(800\ K) = C_{p,M1} - C_{p,M3}(800\ K) = -0.07$ cal mol^{-1} K^{-1} and $\Delta C_{M2-M3}(800\ K) = -0.05$ cal mol^{-1} K^{-1}, are close, even though max M2 ΔV(θ) = 0.08, 0.26, 0.19, and 0.19 kcal mol^{-1}, have nearly half the discrepancy than does M1 from M3 for all four torsions.

The ΔC_{M1-M3} for all five species are plotted in Fig. 7. Figures S3.4–7 provide the information of Fig. 6 for the remaining propane oxidation species. The max absolute ΔV(θ) averaged across the 15 torsions is 0.26 kcal mol^{-1}. Focusing on the methyl and ethyl torsions, by neglecting the C–C–O–O and C–O–O–H torsions, the max absolute ΔV(θ) diminishes to 0.13 kcal mol^{-1} on average. We see from propane and the *n*-propyl radical, shown in Figures S3.4 and S3.5, that such shifts on methyl and ethyl profiles result in heat capacity and entropy shifts of less than 0.01 cal mol^{-1} K^{-1} per torsion at temperatures over 500 K. This distinction is important, because only the number of ethyl and methyl torsions scale with system size in this species set. The near negligible sensitivity of C_p and S to M1 methyl and ethyl torsional profiles when compared to M3, suggests that C_p and S uncertainty from using the more affordable electronic structure method on the scans, will not scale significantly with molecular size. Steric hindrance should not amplify methyl sensitivity in larger species because the medium to high temperature range fa-

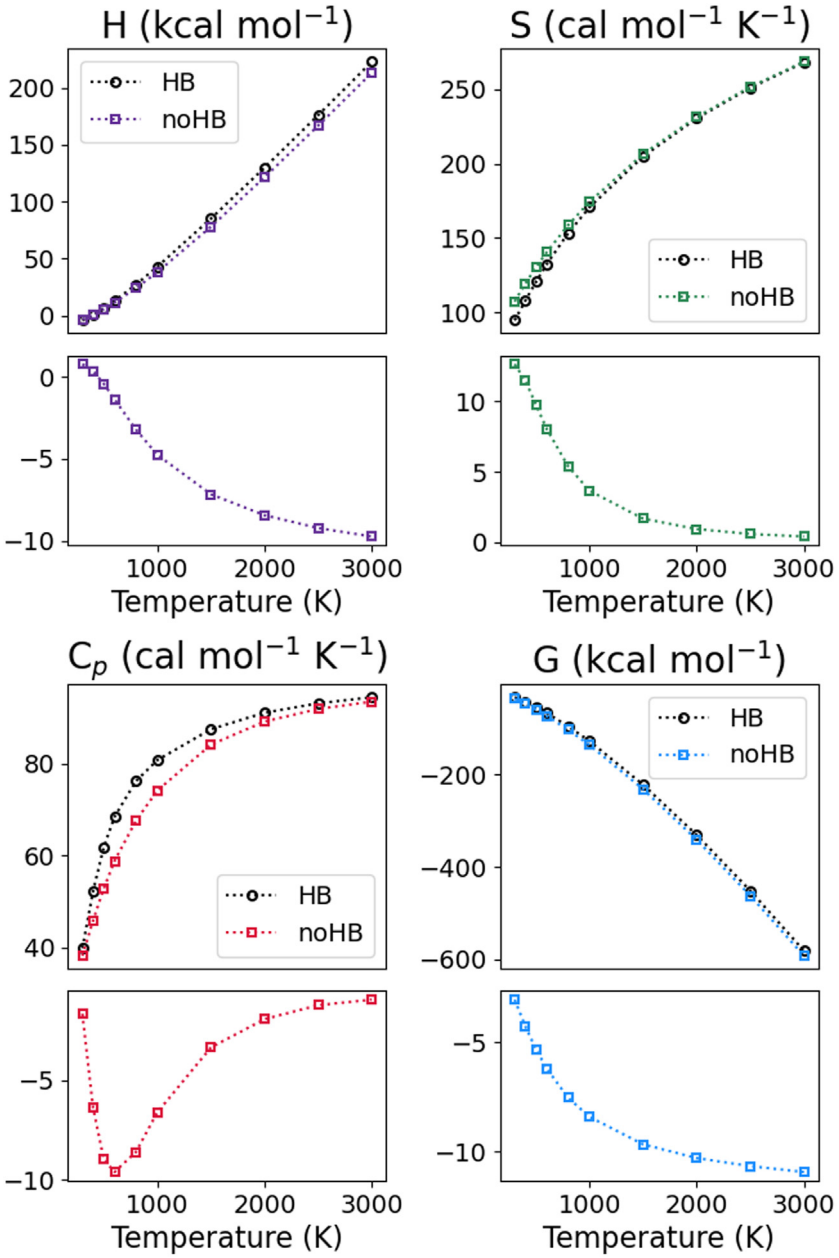

Fig. 5. The enthalpy (top-left, purple), entropy (top-right, green), heat capacity (bottom-left, red), and Gibbs energy (bottom-right, blue) of *n*-pentyl hydroperoxy radical (SMILES, [CH_2]CCCCOO), for the lowest energy hydrogen bonded (HB) and non-hydrogen bonded (nonHB) rotamer. For each property, the absolute thermochemistry for the HB and nHB conformers are provided in the top panel and the difference of the properties (HB - nHB) are in the bottom panel.

vors open configurations. For hydrocarbon species, the uncertainty should remain below 0.10 cal mol^{-1} K^{-1} for both properties above 800 K. For **RO_2H, $R\dot{O}_2$**, and **$\dot{Q}OOH$** species this uncertainty may increase to 0.3 and 0.5 cal mol^{-1} K^{-1}, for S and C_p, respectively. The 800 K Gibbs energy uncertainty due to the choice of electronic structure method used for V(θ), then, is below 0.3 kcal mol^{-1}. We explore further uncertainties from the 1DHR framework in Sections 3.4.3 and 3.6.

3.4. Validation for alkane thermodynamics

3.4.1. Experimental dataset

Both the frequency-dependent scaling factors and the torsional profile scaling factors that are used in the **STAR-1D** method are directly determined from theoretical calculations and are motivated to better represent higher order theoretical descriptions of the partition functions. They are, as such, not directly tailored to improve thermodynamic properties. Nevertheless, when the parameters that build the partition function are more correct, the thermodynamic properties that are derivatives of it should be as well. To understand the extent of the improvement to thermodynamic properties, and their sensitivity to **STAR-1D** routines, we have collated experimental data for alkane species.

The experimental dataset is comprised of C_1–C_7 linear and C_4–C_6 branched alkane species. From the CRC Handbook [78] we obtain entropies (S) for ethane and propane in the temperature range 300–1500 K. From Sinke and coworkers [79] we compile entropies for *n*-butane, *n*-hexane, and *n*-heptane at 300, 500, 700, and 1000 K. From NIST [80] we find heat capacities (C_p) for ethane, propane, *n*-butane, *n*-pentane, and *n*-hexane in the temperature range 300 to 1500 K. For all of these species, along with *i*-butane, *neo*-pentane, 2-methylbutane, 2,3-dimethylbutane,

Table 2
The difference in Gibbs energy ($\delta\Delta G = \Delta G_{nHB} - \Delta G_{HB}$) in kcal mol^{-1}.

SMILES	reference		$\delta\Delta G$[a]			
	r_{HB}[b]	$\angle_{HB}$[c]	300	500	1000	2000
C[CH]CCCOO	2.06	148.40	−3.49	−4.86	−6.29	−6.31
OOC(CC([CH$_2$])(C)C)(C)C	2.07	145.75	−0.59	−1.24	−2.63	−4.16
[CH$_2$]CC(COO)(C)C	2.08	143.84	−2.83	−4.19	−6.03	−7.58
OOCCC(C)(C)[CH$_2$]	2.08	144.83	−3.89	−6.10	−9.45	−12.22
CC(OO)CC[CH$_2$]	2.10	142.67	−2.15	−3.12	−4.68	−6.06
OOCCC([CH$_2$])C	2.11	144.16	−3.22	−4.20	−5.30	−5.61
OOCC(C[C](C)C)C	2.19	143.30	−2.47	−4.10	−6.18	−7.32
OOC(C([CH$_2$])(C)C)C	2.25	119.85	−1.84	−2.53	−3.26	−3.85
[CH$_2$]CCCCOO	2.27	155.87	−3.03	−5.31	−8.42	−10.31
OOCC([C](C)C)C	2.27	125.69	−2.52	−3.62	−4.80	−5.52
OOC(C([CH$_2$])C)C(C)C	2.30	120.31	−0.85	−2.22	−4.56	−6.71
C[CH]C(COO)(C)C	2.31	121.55	−2.11	−3.58	−5.42	−7.19
OOC(C(C)(C)C)C(C)[CH$_2$]	2.31	119.38	−1.30	−2.07	−3.23	−4.56
OOC(CC([CH$_2$])C)(C)C	2.31	136.12	−0.31	−1.52	−3.44	−5.06
OOCC(C([CH$_2$])C)C	2.32	136.88	−1.50	−2.53	−3.97	−4.91
OOCC(CC([CH$_2$])(C)C)C	2.32	155.88	−0.80	−2.22	−4.43	−4.81
CC[CH]CCOO	2.32	121.13	−1.68	−2.20	−2.67	−2.81
CC([CH]C)COO	2.34	120.91	−1.16	−1.69	−2.39	−3.01
CCC(COO)([CH$_2$])C	2.34	118.72	−2.15	−3.29	−4.68	−5.83
OOCC([CH]C(C)C)(C)C	2.35	119.86	−1.95	−3.54	−5.66	−7.47
CC(OO)C[CH$_2$]	2.36	117.09	−0.36	−0.44	−0.59	−0.91
CC(C[CH$_2$])COO	2.37	134.53	−1.53	−2.34	−3.43	−4.22
OOCC([CH$_2$])(C)C	2.37	116.98	−1.98	−2.74	−3.27	−3.49
OOCC([CH]C(C)C)C	2.37	120.22	−2.77	−4.02	−6.28	−9.07
[CH$_2$]CCCOO	2.39	134.76	−1.45	−1.85	−2.20	−2.49
OOCC(CC(C)C)([CH$_2$])C	2.40	116.58	−3.07	−4.28	−6.29	−8.45
OOC(CC(C)C)([CH$_2$])C	2.40	117.57	−0.59	−1.31	−2.90	−4.90
OOC(CC(C)C)(C)C	2.41	116.87	−0.66	−1.58	−2.84	−3.60
OOC(CC(C)(C)C)([CH$_2$])C	2.42	114.99	−1.18	−2.26	−4.39	−7.20
OOC(C([CH$_2$])(C)C)C(C)C	2.42	118.05	−0.68	−1.82	−3.93	−6.15
OOCC([CH$_2$])C	2.43	114.54	−1.86	−2.49	−3.08	−3.48

[a] Temperatures are in Kelvin.
[b] The HB bond length (Å) of the shortest HB in the **STAR-1D** reference conformer.
[c] The angle (in degrees) between atoms in the HB of the reference conformer.

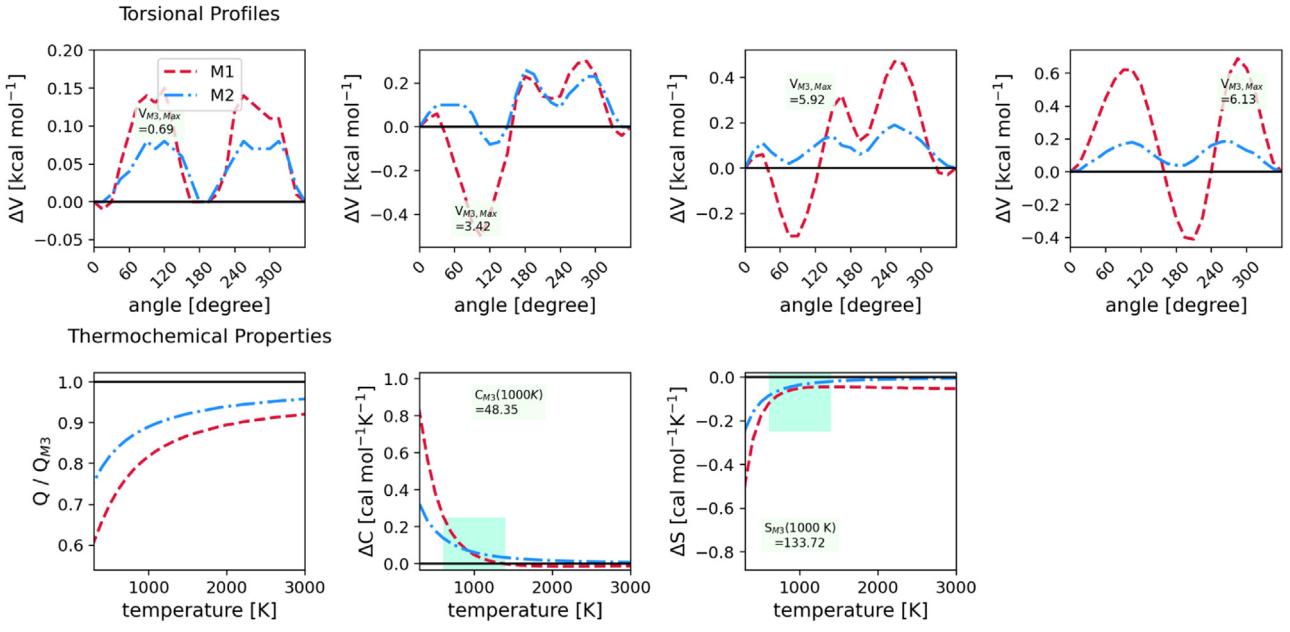

Fig. 6. Comparison of methods M1, M2, and M3, which are identical apart from their torsional profiles, which are computed with M1 = ωB97X-D/cc-pVTZ, M2 = B2PLYP-D3/cc-pVTZ, and M3 = CCSD(T)-F12/cc-pVTZ-F12//B2PLYP-D3/cc-pVTZ.
Top: relative torsional profiles $\Delta V = V_{M1}(\theta)$-$V_{M3}(\theta)$, in red, and $V_{M2}(\theta)$-$V_{M3}(\theta)$, in blue, for rotors D1, D2, D3, and D4 of *n*-propyl hydroperoxy radical, which are defined in Figure S3.3(e). The maximum potential, at M3, is given as $V_{M3,Max}$.
Bottom-left: relative partition functions Q_{M1}/Q_{M2} and Q_{M2}/Q_{M3}.
Bottom-center: relative heat capacities $\Delta C = C_{p,M1} - C_{p,M3}$ and $\Delta C = C_{p,M2} - C_{p,M3}$.
Bottom-right: relative entropies $\Delta S = S_{M1} - S_{M3}$ and $S_{M2} - S_{M3}$. Teal areas highlight sensitive regions for combustion modeling.

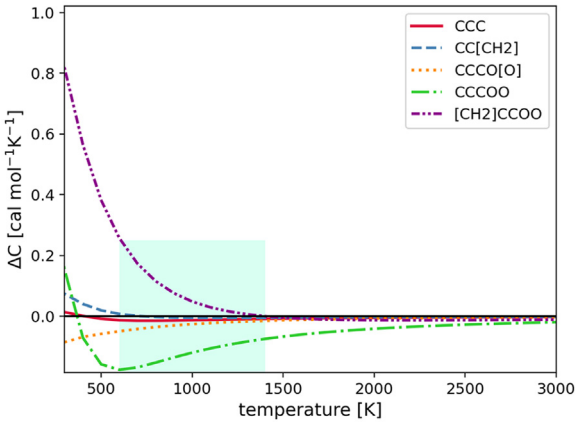

Fig. 7. Relative heat capacities ($\Delta C = C_{p,M1} - C_{p,M3}$) for propane oxidation, where M1 is ωB97X-D/cc-pVTZ and M3 is CCSD(T)-F12/cc-pVTZ-F12//B2PLYP-D3/cc-pVTZ.

2,2-dimethylbutane, and *n*-heptane, the API tables [81] provide extrapolation data for both S and C_p in the temprature range 300 to 1500 K. This latter source has inconsistencies with the other datasets, especially at high temperatures. Comparisons are only made here to Refs. [78–80], with the exception of methane, for which we use API data [81]. The supporting information carries out further comparisons to the API tables [81] in Section S4.2.

3.4.2. Frequency scaling

The RRHO + 1DHR partition function has several limitations when applied to combustion systems. At the high temperatures relevant to combustion chemistry neglecting anharmonicities can lead to significant error. Anharmonic partition function evaluations [58,82], while feasible for small systems, are costly for large molecules. In Section 2.4 we developed a procedure to scale the harmonic frequencies that successively build up the vibrational partition function. In doing so, we determined that 2σ=1.4% for each of our scaled frequencies, which for our largest species would propagate to $2\sigma(Q)$=11% for the product of the frequencies of a species. An 11% uncertainty in a partition function translates to $2\sigma(G) = k_B T \ln(1.11)$ uncertainty in the Gibbs free energy, which is 0.2 kcal mol^{-1} at 800 K and 0.3 kcal mol^{-1} at 1500 K. We here compare to experimental values for C_1–C_6 linear alkanes to empirically explore how the frequency scaling translates into thermodynamic properties.

For the example of propane, we see errors in both the entropies and heat capacities of up to 1 cal mol^{-1} K^{-1} at high temperatures when we use the original RRHO + 1DHR partition function, which is the gray dash-dotted line and the gray x markers in Fig. 8. When we apply our frequency scale factor, the dotted red line, the error for both properties is severely mitigated, with the maximum discrepancies reduced to 0.25 cal mol^{-1} K^{-1}. This trend continues over the C_1–C_6 linear alkanes, shown in Figures S4.8–19. For these molecules, and over the temperature ranges 1200–1500 K, the mean absolute deviation (MAD) for the heat capacities is 0.40 cal mol^{-1} K^{-1} for the scaled frequency RRHO + 1DHR partition function. The entropy MAD is 0.15 cal mol^{-1} K^{-1}, although the tests for high temperature are somewhat limited since CRC Handbook [78] and Stull et al. [79] only have data in the temperature range 1200–1500 K for methane, ethane, and propane. These errors are consistent with the simple propagation of the 1.4% uncertainties in the scaled frequencies. We here note that this method of characterizing anharmonicity through scaled frequencies is expected to break down at high temperatures (e.g., > 1500 K) [65].

3.4.3. Torsional profile scaling

A second limitation of the unscaled RRHO + 1DHR approach is that the harmonic portion of the torsional profiles produced with single-rotor constrained optimized geometries do not map correctly to the harmonic frequencies. This is a consequence of, in part, treating the torsions as fully separable, and, in part, the fact that the 30 degree step sizes about the torsional minima obfuscate the shape of the well. By introducing the potential scaling factor discussed in Section 2.5, we enforce that the set of profiles maps consistently into the harmonic frequencies.

At high temperatures the effect of the hindering potential is largely negligible. Instead, it is when the torsional barrier is on the order of magnitude of $k_B T$, where k_B is the Boltzmann's constant, that the partition function is most sensitive to hindered rotor treatment. The comparison to experimental thermochemistry for propane, in Fig. 8, demonstrates this. We see the blue dashed lines on the left and the blue triangles on the right, are most sensitive to the potential scaling factor in the temperature range 800–900 K. The scaling, for propane, lowers both the heat capacity and the entropy because, in order to map into the harmonic frequencies correctly, the potentials were uniformly elevated. Similarly to the frequency scaling, the entropy shift from the torsional scaling is within 1 cal mol^{-1} K^{-1}. At 800 K, the C_1–C_6 alkane heat capacity RMSD is 1.42 cal mol^{-1} K^{-1} when unscaled and 1.11 cal mol^{-1} K^{-1} with the torsional profile scaling. We provide a final estimate of the uncertainty attributed to the hindered rotor model, however, after more rigorously considering multidimensional effects in Section 3.6.

3.4.4. Dual scaling

The frequency scaling factor and the torsional potential scaling factor are both physically motivated, and importantly, are independent of one another. This is because the potential scaling factor acts on the energies of a torsional profile, and is based on harmonic frequencies. The frequency scale factor aims to approximate the anharmonic character only when building the vibrational partition function for non torsional modes. This allows us to apply both scaling factors simultaneously to the partition function. This is seen as the solid, purple, dual scaling entropy and heat capacities in Fig. 8. The dual scaling for propane removes any temperature dependence of the error, and brings the error for both heat capacity and entropy to within 0.07 cal mol^{-1} K^{-1} for the entire 0–1500 K temperature range. Notably, the underlying scale factors were determined without any recourse to this set of experimental data for the entropy and heat capacity.

Analogous comparisons can be made with experimental data for the linear C_1–C_6 (see Figures S4.8–S4.19). By extending the analysis to the larger alkanes we see that the size of the correction from the torsional scaling directly increases with number of both methyl and, to a greater extent, ethyl rotors. As expected, the effect of frequency scaling is also more pronounced as the size of the molecule increases.

Figure 9 compiles the errors from experiment for heat capacities computed with no scaling in gray, with frequency scaling in red, with torsional potential scaling in blue, and with dual scaling in purple for the six alkane molecules reported in NIST [80], which are the C_1–C_6 linear alkanes. This figure shows clearly the improvement on high temperature heat capacity from the frequency scaling and on low temperature data from potential scaling. For the six species, the dual scaling computed heat capacities have MAD at 300 K, 1000 K, and 1500 K of 0.14, 0.23, and 0.36 cal mol^{-1} K^{-1}, respectively and RMSD of 0.19, 0.34, and 0.52 cal mol^{-1} K^{-1}, respectively. For the full list of 12 species, including data from Scott [81] (see Figure S.4.20–21), the 500 K unscaled heat capacities have MAD = 1.05 and RMSD = 1.13 (see Figure S4.20). Dual scaling diminishes this discrepancy to MAD = 0.16,

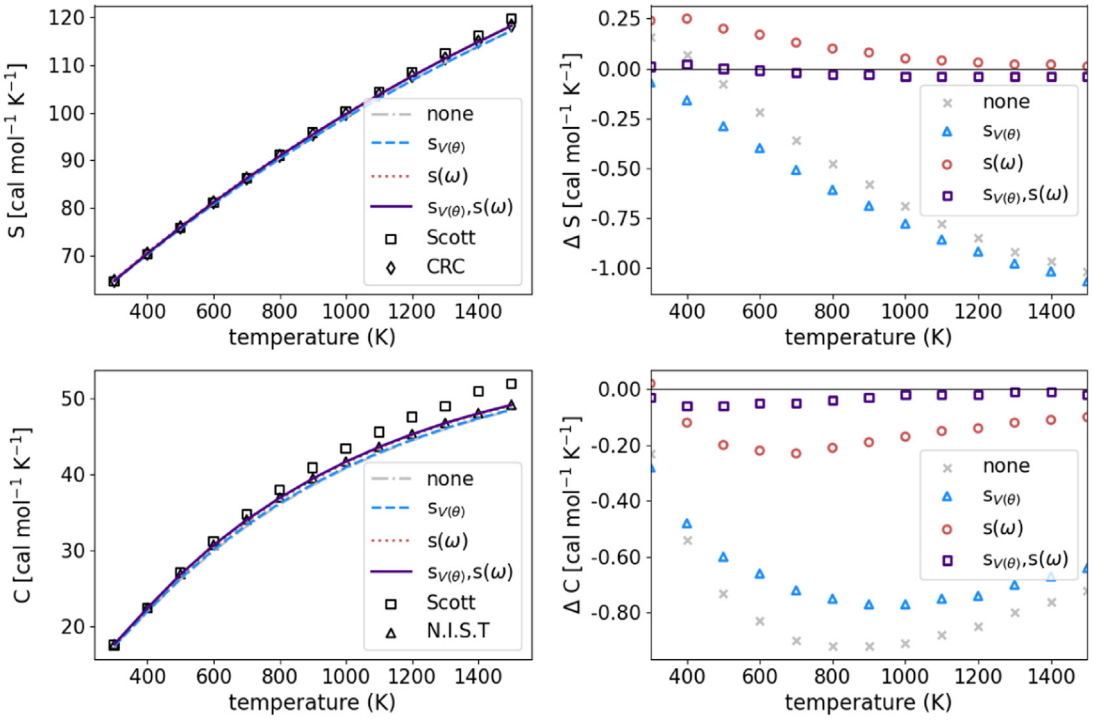

Fig. 8. The entropies, S, (top) and heat capacities, C_p, (bottom) computed for propane plotted alongside experimental data from Scott et al. [81], the CRC Handbook [78] and NIST [80]. The right plots show the difference between the computed and the CRC Handbook S values and the NIST C_p values. Computed values use the **STAR-1D** method, altered by the indicated scaling procedures used. The dash-dotted gray line and cross symbols represent data produced with no scaling, the blue dashed line and triangles applies the torsional scale factor, s_V, the red dotted line and circles applies the frequency-dependent frequency scale factor, s(ω), while the purple line and boxes uses dual scaling to include both s_V, and s(ω), which is the approach in **STAR-1D**.

RMSD = 0.20 cal mol^{-1} K^{-1}. The Scott high temperature data is from extrapolations and is less suited for comparison.

The entropies can be analyzed in a similar manner. Figure 10 compiles the errors from the CRC Handbook [78] or from the Sinke and coworker [79] experimental entropies for each method. Note that only methane, ethane and propane data is present for the boxes at 400, 600, 800, 900, and >1000 K. Even so, the data present shows a dramatic improvement in the temperature dependence of the error and the size of the interquartile range when using the dual scaling. With it, the MAD from the CRC Handbook and Sinke data is within 0.5 cal mol^{-1} K^{-1} across the 300–1500 K temperature range and the median is lower. However, even with the large improvement in the theoretical results from the scaling, there still remains a small negative bias on the heat capacities and a positive bias on the entropies.

3.5. Umbrella motions, torsional profiles, and symmetry

The torsional profile scaling routine relies on the fundamental assumption that a profile will have harmonic behavior about the torsional minimum energy structure. This assumption breaks down if the harmonic region cannot be captured within the chosen step size (i.e., 30 degrees). The 30 degree grid is sufficient for most species, but in the presence of umbrella motions we find that the torsional scan often only partially samples the umbrella inversion near the minimum. As a result of the umbrella motion coupling, the symmetry for the torsional scan is thrown off and the scale factor becomes non-physical. Reducing the step size to 15 or 5 degrees can correct this issue, but not predictably. Instead, we consider a general approach to predict a scale factor for a radical species.

If the torsional potential scaling routine is to capture the multi-dimensional effects on each torsion, we should see a consistent increase in the overall scale factor with each additional rotor. This assertion is visible in Fig. 11. For the **RH** species, Fig. 11(a) the per-torsion scaling factor, however, only increases with number of torsions once it surpasses three torsions. It is intuitive that multi-dimensional effects are more substantial when the molecule has enough torsions to wrap back on itself.

We see by contrasting Fig. 11(a) and (b) that **RH** and **RO$_2$H** species have somewhat disparate behavior. Even within the **RO$_2$H** species there is a spread on each rotor, as different branching patterns and hydroperoxy sites influence the scaling.

The **RȮ$_2$** species in Fig. 11(c) visibly have a similar trend to the **RO$_2$H** species and physically have the same connectivities with one fewer torsion, i.e., ∠C–O–O–H. Because they are the only radical species in our set that do not have potential umbrella motions, they present a unique opportunity to consider what the relationship between a radical and parent molecule scaling factors should be. Figure 12 displays the per-rotor scaling factor for each **RȮ$_2$** species against the scaling factor for its **RO$_2$H** parent. In this context, the scale factor for species with same connectivities are directly related to one another. Somewhat non-intuitively, the presence of a radical produces a greater per-rotor scale factor than the presence of the extra ∠C–O–O–H torsion. Quantitatively, the radical species has a per-rotor scale factor that is $(1.124 - 0.012N_{rotor})$ × the parent species scale factor. **RȮ$_2$** scale factors predicted by this fit have a MAD of 0.06 from the predetermined **RȮ$_2$** scale factor, an uncertainty to V(θ) on the same order as the choice of electronic structure method (see Section 3.3, where the average of MAX($\frac{V_{max,M3}}{V_{max,M1}}$, $\frac{V_{max,M1}}{V_{max,M3}}$) is 1.05 across 15 torsional profiles). To avoid the umbrella motion related ambiguities for the **Ṙ** and **ȮOOH** species, we use this per-rotor scale factor expression in place of Eq. (3) for the present **STAR-1D** evaluations.

Here, we also note that the effective symmetry of the molecule (σ_{eff} in Eq. (1)) must be increased by a factor of two if an um-

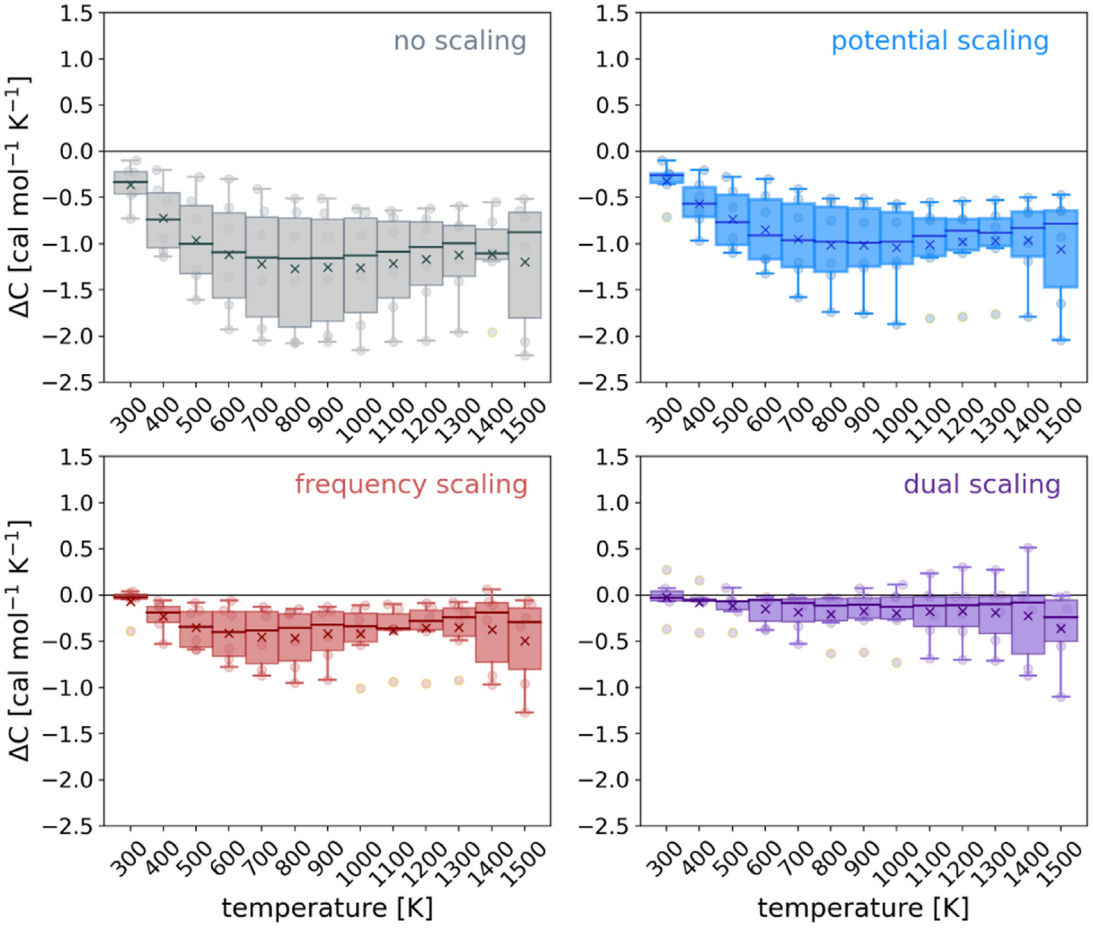

Fig. 9. A box and whisker plot of the difference between computed and experimental heat capacities for C_1–C_6 linear alkanes. Experimental data for methane is from Scott [81], and the remaining alkanes data is from NIST [80]. Each box represents the heat capacity errors, ΔC, for all molecules at a given temperature. Within each box, a horizontal dark line denotes the median error value, and a dark x denotes the mean error value. Each box spreads from the 25th to the 75th percentile of the errors. The whiskers extend out to, and are capped at, the 1.5× interquartile range. Translucent dots give the error for each species at each temperature.

brella inversion is captured in the torsional scan routine. This generally occurs when the four atoms that define the umbrella are between 5 and 17° off planar. The umbrella less predictably inverts when the center is a terminal $\dot{C}H_2$ group. For such species in the **R /Q̇OOH** set we manually look at the torsional scans for symmetry in the profile that corresponds to umbrella inversion and update the symmetry number accordingly. For future data production we currently are developing a procedure in AutoMech to read from the geometry at each scan point to quantitatively identify inversion of the umbrella.

3.6. Multi-dimensional effects

Multi-dimensional effects on thermodynamics are well recognized but rarely treated in combustion systems due to the computational cost of building the multi-dimensional hindered rotor (MDHR) partition function [83]. Torsional coupling is especially relevant in **Q̇OOH** radicals, which have the flexibility to form hydrogen bonds during torsional rotation about backbone atoms. Multi-conformational [84–86] methods aim to capture multi-dimensional effects with RRHO partition functions and corrections to thermodynamic properties based on Boltzmann probability distributions for the conformers. Similarly, the multi-structural method with torsional anharmonicity (MS-T) [87] builds conformational-rovibrational partition functions which requires geometries and Hessians at 3^t configurations, where t is the number of torsions. The Hessians facilitate prediction of torsional barrier heights and torsional anharmonicity factors. Requiring a complete enumeration of the conformational minima, these methods are computationally expensive for molecules with more than a handful of torsional modes.

Several recent works focus on a two dimensional treatment (2DHR), suggesting it is sufficient to capture partial coupling of rotors [88–91]. Applying this to MS-T, Wu et al. treat sets of torsion pairs (MS-2DT) to significantly reduce the dimensionality of MS-T [92]. In doing so they miss conformations that are largely the high-energy structures. MS-T results, however, are most sensitive to computation of the low-energy conformers, and more affordable methods can be used on the high-energy structures [93]. The lost contribution to the partition function from the missed conformers, when using MS-2DT in place of MS-T, increases with species size. For *n*-octane, this contribution is 18–33% from 200–2000 K [92].

Green and coworkers, in a study of alkylperoxy and hydroperoxyalkylperoxy radicals note 1DHR sensitivity to scanning about HB or nHB conformers [50]. They develop a method to sub-divide the dihedral angle phase-space into regions near the HB structures and into a region corresponding to nHB structures. They then solve the HB region with a non-separable rotor, semi-classical, partition function, where methyl rotors are treated separable. All rotors in the nHB region, however, are treated as fully separable. For $HOOCH_2CH(CH_3)O\dot{O}$, this hybrid approach slightly overcorrects the 1DHR enthalpy (which was originally 2 kcal mol^{-1} higher) to 0.5 kcal mol^{-1} lower than the enthalpy from a MDHR partition function (where their MDHR partition function also sep-

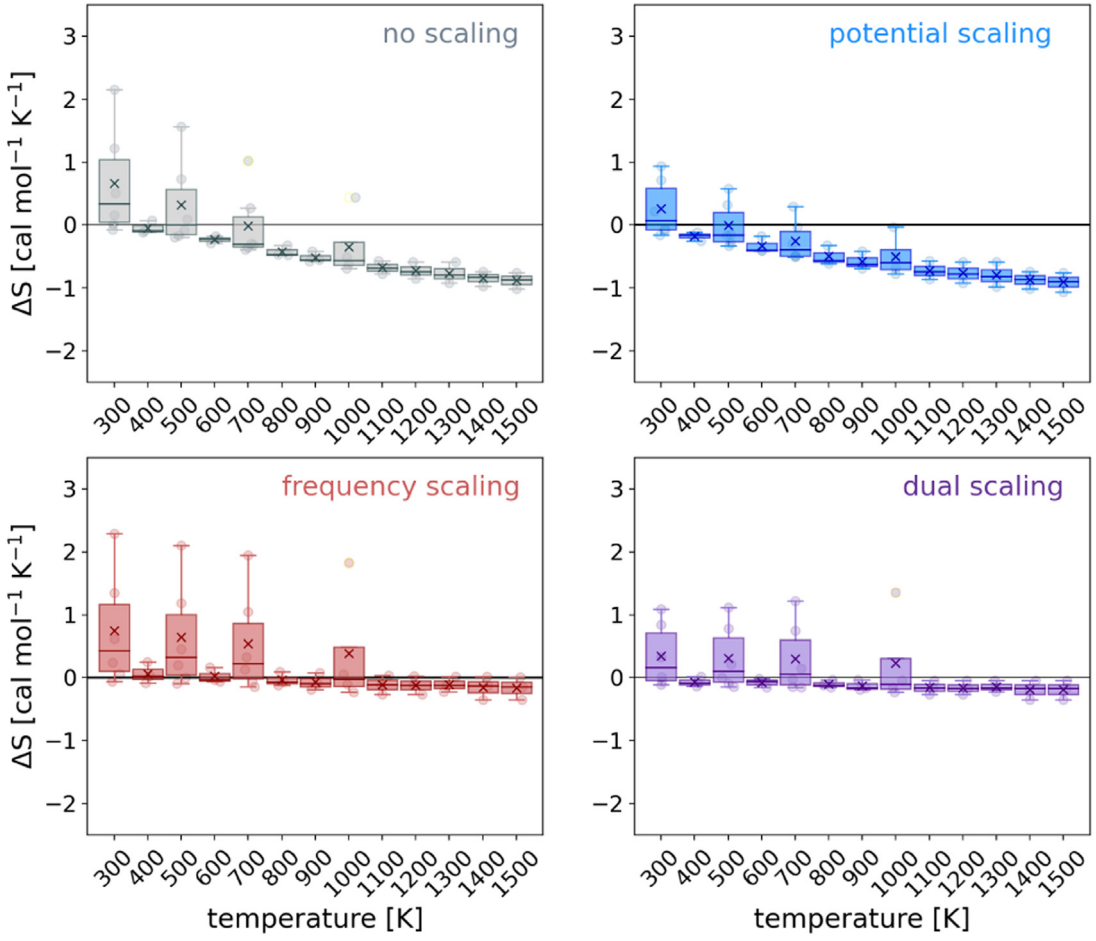

Fig. 10. The difference between computed and experimental entropies for C_1–C_6 linear alkanes. Experimental data for ethane and propane are from Ref. [78], methane is from Ref. [81], and the remaining alkane data is from Ref. [79]. Each box represents the entropy errors, ΔS, for all molecules at a given temperature. Within each box, a horizontal dark line denotes the median error value, and a dark x denotes the mean error value. Each box spreads from the 25th to the 75th percentile of the errors. The whiskers extend out to, and are capped at, the 1.5× interquartile range. Translucent dots give each error individual value.

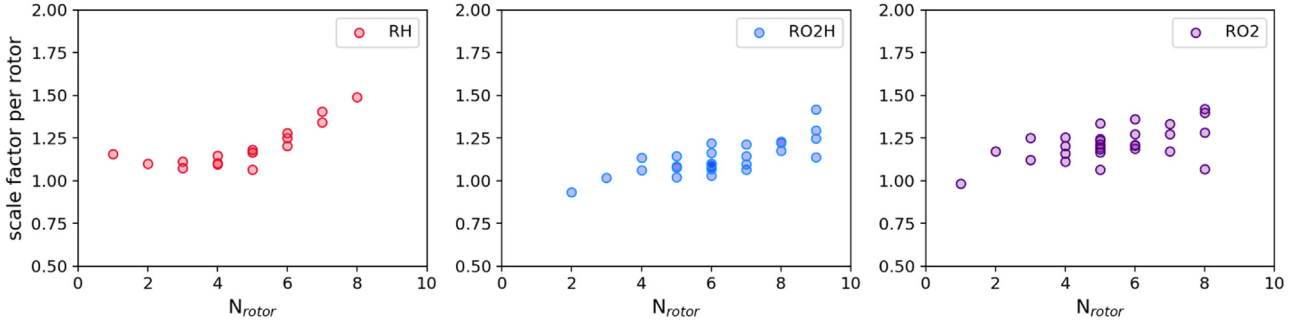

Fig. 11. The torsional profile scaling factor, per torsion, plotted against the number of torsions for (a) **RH**, (b) **RO_2H**, and (c) **$R\dot{O}_2$** species.

arates methyl torsions). When using 1DHR and the hybrid approach, their 298 K entropy difference from a full MDHR result are 2.5 cal mol^{-1} K^{-1} and −3.3 cal mol^{-1} K^{-1}, respectively. The corresponding errors in the 298 K heat capacity are −17.4 cal mol^{-1} K^{-1} and −6.6 cal mol^{-1} K^{-1}, respectively.

These approximations to a full multi-dimensional partition function incompletely and somewhat unpredictably capture multi-dimensional effects. Moreover, they remain costly for more than a few rotors. The **STAR-1D** scaling procedure recovers coupling between torsional motions by correlating the 1D torsional frequency to the coupled vibrational frequencies. In doing so it adds virtually no extra computational costs to the widely used 1DHR approach.

We here evaluated the extent of remaining multi-dimensional effects when using the scaled-1DHR approach by computing MDHR properties for butane (C_4H_{10}), the butyl (C_4H_9) radical, propyl peroxy ($C_3H_5O_2$) radical, ethyl hydroperoxy ($C_2H_4O_2H$) radical, and ethyl hydroperoxide ($C_2H_5O_2H$) with fully multidimensional ωB97X-D/cc-pVTZ scans and contrasting them to the 1DHR partition function computed with scaled one-dimensional ωB97X-D/cc-pVTZ scans. All of these computations were automated with the AutoMech software suite. The five species have a 0.18 kcal mol^{-1} MAD in their 298 K enthalpies between the scaled-1DHR and the MDHR. Their 298 K entropy MAD is 0.20 cal mol^{-1} K^{-1} and the 298 K heat capacity MAD is 0.57 cal mol^{-1} K^{-1}.

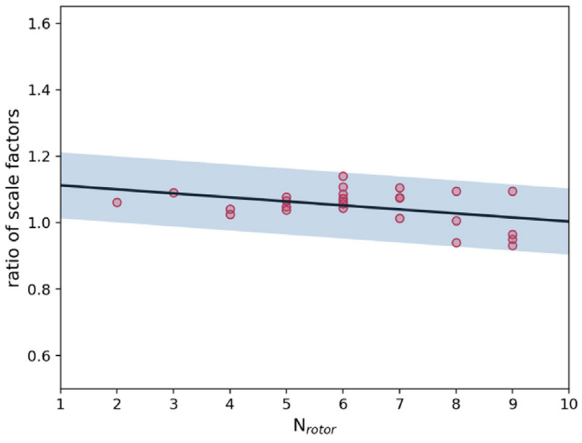

Fig. 12. The ratio between torsional profile per-rotor scaling factors for 26 **RȮ$_2$** and 26 **RO$_2$H** species plotted against the number of torsions. The predicted ratio, the solid black line, is 1.124–0.012 N_{rotor} and has a 2σ=0.1, demonstrated by the shaded area.

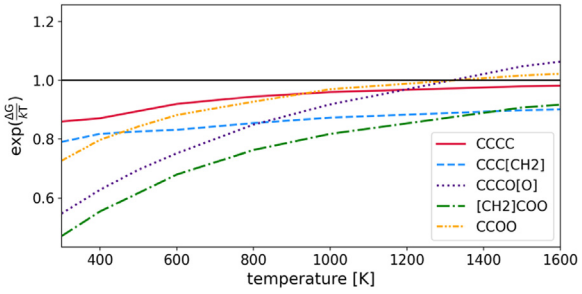

Fig. 13. The influence of multidimensional effects on rates, shown through the Boltzmann factor of the Gibbs energy difference, ΔG, between scaled-1DHR and MDHR partition functions produced with ωB97X-D/cc-pVTZ hindered rotor scans plotted against temperature, T.

Table 3
Heats of formation (ΔH_f) and entropies (S) of alkyl radicals collected from experiment alongside bolded **STAR-1D** results of this work.

	ΔH_f(298 K) kcal mol^{-1}	S(298 K) cal mol^{-1} K^{-1}
C_2H_5	28.92 ± 0.36[a] 28.85 ± 0.24[e] 28.90[d] **28.68**	61.19 ± 1.67[a] – 59.05[d] **59.17**
n-C_3H_7	24.09 ± 0.50[b] 24.21 ± 0.24[e] 24.02[d] **23.98**	67.88 ± 1.20[b] – 69.17[d] **67.91**
i-C_3H_7	21.51 ± 0.41[a] 20.70 ± 0.48[b] 21.15 ± 0.24[e] 21.51[d] **20.82**	69.79 ± 1.20[a] 67.16 ± 1.20[b] – 69.14[d] **69.10**
n-C_4H_9	19.34 ± 0.53[b] 19.24[d] **19.31**	78.63 ± 1.20[a] 79.26[d] **78.82**
s-C_4H_9	16.13 ± 0.53[a,c] 15.94 ± 0.50[b] **16.14**	81.98 ± 2.15[a] 78.87 ± 1.20[b] **80.42**
i-C_4H_9	17.38 ± 0.53[b] 17.38[d] **17.55**	75.53 ± 1.20[b] 76.35[d] **76.06**
t-C_4H_9	12.26 ± 0.43[a] 12.38 ± 0.31[b] 12.26[d] **12.42**	74.81 ± 1.20[a] 75.29 ± 0.96[b] 75.79[d] **76.23**

[a] Seakins et al. 2nd- and 3rd-law determination from R+HBr PI-MS [7].
[b] Seetula et al. 2nd-law determination from R+HBr PI-MS [8].
[c] Seetula et al. 2nd- and 3rd-law determination from R+HI PI-MS [6].
[d] Baulch et al. recommended thermochemical data from compilation of experimental, ab initio, and group additivity methods [95].
[e] Bodi et al. RCH_2NH_2 TPEPICO dissocation energies with CBS-APNO [94].

More interestingly, we predict the influence of the thermochemistry on rates and equilibrium constants by considering the differences in the scaled-1DHR and MDHR Gibbs energy in a Boltzmann factor, exp $\frac{\Delta G}{kT}$, in Fig. 13. At combustion temperatures the remaining multi-dimensional effects cause less than a 25% impact on the rates. The low temperature properties are more sensitive to multi-dimensional effects, as expected, but still remain within a factor of 2. The MAD of the Gibbs energy at 800 K is 0.23 kcal mol^{-1}, where $C_2H_4O_2H$ has the max deviation of 0.44 kcal mol^{-1}. Note that this 800 K deviation is the largest deviation across all temperatures, owing to the sensitivity of thermodynamic properties to hindered rotors in this temperature region.

As species grow larger and generate more low-frequency motions, their rotor coupling will increase. While the alkane oxidation species have up to 9 torsional modes, the maximum number of non-methyl torsions in the present dataset is 5. Noting that methyl groups rarely experience strong coupling, we double the max deviation from our species with 3 torsion to estimate a max of 0.8 kcal mol^{-1} uncertainty in Gibbs energies due to multidimensional effects in the largest molecules.

3.7. Uncertainty

This section considers the cumulative effect of the various assumptions made in the **STAR-1D** protocol. Several are associated with uncertainties in electronic structure parameters. From the CBH-ANL ΔH_f(0 K), for example, we have a 0.2–0.5 kcal mol^{-1} uncertainty that directly applies to the Gibbs energy. We have also considered the translation of deviations in our scaled frequencies from anharmonic frequencies into uncertainties in thermodynamic properties to establish an uncertainty within 0.4 kcal mol^{-1} in the ΔG(800 K). The 1D ωB97X-D/cc-pVTZ torsional scans produced uncertainties in the ΔG(800 K) of 0.3 kcal mol^{-1} when compared to thermochemistry from scans at higher levels of theory. Finally, we consider uncertainties due to the thermodynamic model– more specifically, we examine the multi-dimensional effects. The **STAR-1D** scaling procedure was able to recover some rotor coupling to leave a remaining uncertainty in ΔG(800 K) due to multi-dimensional effects of 0.8 kcal mol^{-1}. The presence of umbrella modes would increase this uncertainty to 1.0 kcal mol^{-1}. Due to the complexity of the functional dependence of the Gibbs energy on each of these uncertainty sources, and our generous assignments for each of them, we simply propagate the error with an assumption that the component errors are uncorrelated to obtain a final 800 K uncertainty of 1.2 kcal mol^{-1}.

For the large and less branched **ȮOOH** species there remains more ambiguity in our uncertainty estimates. For the **ȮOOH** species we use the lowest electronic energy, non-hydrogen bonded conformer as suitable across the entire temperature range. At any specific higher temperature, a different conformer might be a more appropriate reference conformer.

For smaller molecules, and for closed shell species, the uncertainties are much smaller, perhaps 0.6 kcal mol^{-1}. Indeed, for the six linear alkane species discussed in Section 3.4.2 we are very well within even such a reduced uncertainty in comparison to experimental measurements.

Table 4
STAR-1D heat of formation (ΔH_f) in kcal mol^{-1} and entropy (S) and heat capacities (C_p) in cal mol^{-1} K^{-1} for alkane and alkyl radicals. Temperatures are in Kelvin.

SMILES	ΔH_f	S	C_p									
	298	298	300	400	500	600	800	1000	1500	2000	2500	3000
RH												
C	−15.91	44.46	8.52	9.65	11.04	12.44	15.00	17.13	20.66	22.55	23.60	24.22
CC	−20.23	54.67	12.53	15.58	18.57	21.27	25.77	29.27	34.86	37.75	39.35	40.30
CCC	−25.27	64.62	17.64	22.41	26.85	30.71	36.95	41.71	49.19	53.04	55.16	56.42
CC(C)C	−32.22	70.52	23.30	29.80	35.69	40.69	48.60	54.51	63.73	68.45	71.04	72.59
CCCC	−30.13	74.46	23.28	29.41	35.12	40.08	48.07	54.10	63.52	68.30	70.97	72.47
CC(C)(C)C	−40.19	73.46	29.19	37.48	44.88	51.09	60.69	67.71	78.53	84.03	87.05	88.84
CCC(C)C	−36.60	82.47	28.83	36.68	43.82	49.92	59.60	66.82	78.02	83.72	86.84	88.73
CCCCC	−34.96	84.24	28.90	36.42	43.46	49.54	59.27	66.57	77.90	83.65	86.89	88.67
CC(C(C)C)C	−41.94	88.04	34.43	43.74	52.14	59.30	70.64	79.12	92.28	98.97	102.66	104.77
CCC(C)(C)C	−44.02	85.84	34.34	44.09	52.84	60.21	71.66	79.98	92.85	99.32	102.87	104.94
CCCCCC	−39.81	93.92	34.51	43.55	52.01	59.28	70.76	79.31	92.45	99.10	102.72	104.91
CC(CC(C)C)C	−48.24	93.40	41.77	53.89	63.95	72.10	84.52	93.69	107.83	114.99	118.97	121.22
CCC(C(C)C)C	−46.47	96.97	40.84	52.62	62.72	71.01	83.70	93.03	107.52	114.85	118.87	121.20
CCCCCCC	−44.67	103.46	40.22	50.77	60.67	69.15	82.44	92.20	107.15	114.56	118.67	121.12
CC(C(C)C)C(C)C	−51.95	100.29	46.49	59.87	71.55	81.26	96.06	106.70	122.77	130.78	135.16	137.74
CC(CC(C)(C)C)C	−53.51	100.51	44.95	58.08	70.00	80.04	95.42	106.43	122.83	130.87	135.26	137.75
Ṙ												
[CH_3]	35.03	46.51	9.41	10.15	10.89	11.59	12.92	14.11	16.31	17.56	18.28	18.72
C[CH_2]	28.68	59.17	12.26	14.79	17.21	19.37	22.95	25.75	30.28	32.65	33.97	34.75
CC[CH_2]	23.98	67.91	17.41	21.59	25.42	28.72	34.05	38.12	44.57	47.91	49.75	50.85
C[CH]C	20.82	69.10	16.28	20.22	24.09	27.55	33.26	37.55	44.32	47.78	49.67	50.80
CC(C)[CH_2]	12.42	76.23	21.72	26.70	31.74	36.30	43.82	49.55	58.45	62.95	65.44	66.80
CC([CH_2])C	17.55	76.06	23.08	28.98	34.23	38.66	45.63	50.85	59.02	63.25	65.68	67.00
CCC[CH_2]	19.31	78.82	22.86	28.62	33.84	38.30	45.37	50.68	58.99	63.25	65.60	67.02
C[CH]CC	16.14	80.42	21.80	27.22	32.40	36.93	44.34	49.91	58.61	63.03	65.46	66.96
C[C](C)C	12.14	85.08	28.73	36.18	42.85	48.48	57.23	63.70	73.69	78.77	81.57	83.23
CC(C)(C)[CH_2]	10.11	78.46	28.86	36.56	43.33	48.97	57.68	64.00	73.82	78.84	81.60	83.25
CC(C)([CH_2])C	8.21	87.02	26.85	33.47	39.93	45.65	54.91	61.88	72.70	78.17	81.17	82.94
CC([CH_2])(C)C	11.92	88.90	26.84	34.00	40.63	46.32	55.46	62.31	72.85	78.27	81.32	82.84
CCC([CH_2])C	12.92	87.18	28.25	35.76	42.46	48.09	56.89	63.40	73.46	78.62	81.48	83.10
CCCC[CH_2]	14.37	86.81	28.71	35.91	42.43	47.98	56.74	63.26	73.44	78.62	81.47	83.22
C[CH]C(C)C	9.96	86.97	27.71	34.78	41.34	46.99	55.93	62.67	73.09	78.40	81.31	83.05
C[CH]CCC	11.30	89.41	27.16	34.38	41.05	46.79	55.89	62.68	73.15	78.46	81.40	83.08
[CH_2]CC(C)(C)C	4.57	88.65	33.98	43.32	51.62	58.57	69.21	76.87	88.54	94.41	97.55	99.55
CC[CH]CCC	6.50	99.31	32.53	41.44	49.49	56.40	67.24	75.26	87.61	93.80	97.17	99.33
CCC([CH_2])(C)C	6.00	89.68	34.69	43.71	51.74	58.48	68.93	76.57	88.30	94.27	97.49	99.45
C[C](C(C)C)C	2.22	93.63	32.58	40.83	48.59	55.39	66.21	74.41	87.11	93.39	96.83	99.05
C[CH]C(C)(C)C	2.75	90.65	33.19	42.16	50.30	57.20	67.92	75.78	87.94	93.92	97.27	99.22
C[CH]CCCC	6.31	98.53	33.07	41.78	49.78	56.62	67.40	75.39	87.71	93.88	97.23	99.30
CC(C(C)C)[CH_2]	7.26	93.67	34.49	43.29	51.11	57.75	68.09	75.81	87.81	93.93	97.29	99.38
CCCCC[CH_2]	9.52	97.66	34.39	43.03	50.94	57.66	68.19	75.97	87.94	94.02	97.38	99.32
[CH_2]CC(C(C)C)C	2.34	100.72	41.19	51.71	60.93	68.64	80.56	89.33	102.86	109.70	113.43	115.58
CC([CH]C(C)C)C	−0.98	101.86	39.14	49.60	58.99	66.87	79.17	88.24	102.11	109.14	112.99	115.38
CC[CH]CCCC	2.26	109.53	39.35	49.53	58.86	66.75	79.07	88.20	102.22	109.26	113.06	115.37
CCC(C(C)C)[CH_2]	2.41	101.14	40.12	50.81	60.38	68.37	80.62	89.50	103.04	109.85	113.58	115.74
CCC[CH]CCC	2.03	108.99	38.39	48.88	58.48	66.65	79.22	88.32	102.42	109.43	113.23	115.49
C[C](CC(C)C)C	−4.15	100.45	38.25	48.61	58.10	66.17	78.77	88.00	102.12	109.20	113.08	115.44
C[CH]C(C(C)C)C	−0.44	101.57	39.83	49.84	59.07	66.95	79.32	88.43	102.39	109.48	113.20	115.58
C[CH]CCCCC	1.91	109.07	38.73	48.90	58.34	66.36	78.97	88.15	102.21	109.37	113.16	115.44
CC(CC(C)C)[CH_2]	1.58	100.87	41.84	52.44	61.54	69.06	80.78	89.45	102.80	109.67	113.37	115.61
C[C](C(C)C)C	−1.98	103.99	38.30	48.26	57.54	65.55	78.09	87.39	101.66	108.94	112.87	115.23
CCC([C](C)C)C	−2.87	101.28	38.71	48.67	57.99	66.04	78.70	88.01	102.20	109.25	113.17	115.42
CCC(C(C)[CH_2])C	2.64	99.66	41.36	52.57	61.97	69.57	81.17	89.70	103.02	109.78	113.50	115.69
CCCCCC[CH_2]	4.66	107.29	40.07	50.19	59.55	67.44	79.78	88.80	102.62	109.56	113.28	115.53
[CH_2]C(C(C)C)C(C)C	−3.83	100.94	45.87	59.64	71.83	81.66	95.73	105.26	119.33	126.37	130.14	132.52
C[C](C(C)C)C(C)C	−8.23	104.95	43.91	56.47	67.87	77.40	91.79	102.04	117.30	125.06	129.27	131.76
C[C](CC(C)(C)C)C	−11.56	104.36	43.47	55.69	66.99	76.61	91.44	102.01	117.67	125.38	129.56	131.92
CC([C](C)C)C(C)C	−8.79	106.76	44.39	55.96	66.76	76.04	90.57	101.17	117.17	125.03	129.32	131.87
CC([CH]C(C)(C)C)C	−8.36	104.36	45.65	58.18	69.39	78.72	92.78	102.77	117.72	125.30	129.50	131.87
CC(C([CH_2])C)C(C)C	−3.05	103.24	46.96	60.50	72.01	81.18	94.52	103.92	118.32	125.70	129.78	132.16
CC(CC([CH_2])(C)C)C	−4.30	102.88	47.98	60.41	71.28	80.32	94.10	103.94	118.71	126.05	129.97	132.28
CC(CC(C)(C)C)[CH_2]	−4.47	104.37	46.18	58.58	69.61	78.84	92.93	103.13	118.17	125.69	129.77	132.17

3.8. Validation for radical species

Validating against experimentally determined reaction thermochemistry is key to evaluating the reliability of the **STAR-1D** method. In Section 3.4 we demonstrated the success of **STAR-1D** in predicting entropy and heat capacity for six linear alkane species. We here evaluate our consistency with experimental findings for remaining species types in the alkane oxidation system. The set, for instance, contains several branching and radical substitution patterns for alkyl radicals that exist in literature. Seakins et al. [7] and Seetula et al. [6,8] estimated heats of formation and entropies, using second- and third-law methods, from **Ṙ** + **HX** ⇌ **RH** + **X**. These studies were performed in heatable tubular reactors coupled to photoionization mass spectrometry (PI-MS) [6–8].

Table 5
STAR-1D heat of formation (ΔH_f) in kcal mol^{-1} and entropy (S) and heat capacities (C_p) in cal mol^{-1} K^{-1} for hydroperoxide species and peroxy radicals. Temperatures are in Kelvin.

SMILES	ΔH_f	S	C_p									
	298	298	300	400	500	600	800	1000	1500	2000	2500	3000
RO_2H												
COO	−30.39	66.32	14.62	17.06	19.34	21.31	24.44	26.78	30.48	32.41	33.49	34.10
CCOO	−38.32	75.90	20.04	24.20	27.91	31.02	35.87	39.44	44.98	47.82	49.38	50.31
CCCOO	−42.93	85.09	26.58	32.10	36.94	41.01	47.38	52.11	59.46	63.21	65.27	66.51
OOC(C)C	−47.19	82.60	26.25	31.88	36.84	41.00	47.43	52.15	59.45	63.19	65.24	66.46
CCCCOO	−47.73	94.98	32.09	39.05	45.24	50.45	58.60	64.60	73.86	78.56	81.08	82.64
CC(OO)CC	−51.76	93.43	32.37	39.21	45.32	50.50	58.58	64.54	73.75	78.45	81.03	82.56
OOC(C)(C)C	−56.56	86.36	32.34	39.74	46.08	51.30	59.27	65.08	74.03	78.62	81.14	82.64
OOCC(C)C	−49.72	91.00	33.66	40.51	46.35	51.24	58.97	64.77	73.86	78.48	81.09	82.64
CC(CC)COO	−54.02	102.04	39.20	47.49	54.63	60.65	70.15	77.23	88.25	93.86	96.87	98.72
CCCCCOO	−52.62	104.74	37.60	46.13	53.76	60.16	70.09	77.36	88.44	93.99	97.00	98.86
CC(OO)CCC	−56.40	101.72	38.63	47.30	54.81	61.07	70.71	77.77	88.61	94.10	97.10	98.91
CCC(OO)(C)C	−60.70	96.68	39.30	48.05	55.54	61.69	71.06	77.89	88.50	93.95	96.97	98.80
CCC(OO)CC	−56.17	100.40	40.00	47.80	54.83	60.84	70.31	77.34	88.26	93.86	96.92	98.78
OOC(C(C)C)C	−57.49	98.41	39.79	48.35	55.48	61.37	70.58	77.45	88.28	93.89	96.89	98.72
OOCC(C)(C)C	−57.47	96.23	37.20	45.85	53.61	60.13	70.16	77.44	88.50	94.09	97.09	98.87
OOCCC(C)C	−54.18	101.57	37.82	46.41	54.05	60.43	70.26	77.43	88.41	93.96	97.07	98.85
CCC(COO)(C)C	−61.15	105.80	44.76	54.46	63.25	70.70	82.24	90.61	103.31	109.68	113.13	115.17
OOC(C(C)(C)C)C	−64.53	102.11	44.36	54.61	63.48	70.89	82.32	90.66	103.35	109.71	113.16	115.22
OOC(C(C)C)(C)C	−66.03	101.75	45.11	55.91	64.93	72.22	83.15	91.03	103.20	109.49	112.94	114.97
OOCC(C(C)C)C	−59.58	107.89	44.93	55.17	63.83	70.95	82.01	90.10	102.80	109.23	112.74	114.87
OOCCC(C)(C)C	−61.03	101.85	44.83	54.95	64.11	71.84	83.68	92.09	104.51	110.60	113.85	115.62
$R\dot{O}_2$												
CO[O]	2.96	64.48	12.03	14.13	16.21	18.04	20.95	23.09	26.36	27.98	28.91	29.45
CCO[O]	−5.56	74.08	17.70	21.45	24.89	27.81	32.35	35.67	40.76	43.36	44.74	45.57
[O]OC(C)C	−14.73	81.05	24.07	29.27	33.85	37.71	43.73	48.19	55.06	58.60	60.49	61.67
CCCO[O]	−10.23	83.57	23.34	28.69	33.55	37.64	43.90	48.43	55.30	58.75	60.64	61.78
CCCCO[O]	−15.04	93.17	29.30	35.98	42.10	47.26	55.20	60.97	69.71	74.07	76.46	77.97
[O]OC(C)(C)C	−24.51	84.70	30.55	37.46	43.32	48.15	55.60	61.09	69.63	74.00	76.37	77.83
[O]OCC(C)C	−16.96	89.97	29.67	36.33	42.44	47.57	55.44	61.13	69.77	74.08	76.47	77.92
CC(O[O])CC	−19.42	91.60	29.74	36.48	42.46	47.47	55.21	60.88	69.61	73.99	76.38	77.91
CC(CC)CO[O]	−21.18	100.87	35.71	43.54	50.80	56.98	66.58	73.56	84.19	89.45	92.34	94.04
CCCCCO[O]	−19.89	102.75	35.11	43.20	50.70	57.03	66.76	73.75	84.32	89.58	92.42	94.03
[O]OC(C(C)C)C	−25.12	97.39	36.67	44.58	51.65	57.56	66.84	73.64	84.11	89.39	92.29	94.02
[O]OCC(C)(C)C	−24.80	93.66	34.14	43.15	51.09	57.63	67.44	74.37	84.67	89.77	92.56	94.17
[O]OCCC(C)C	−21.50	99.62	35.37	43.61	51.02	57.25	66.85	73.73	84.27	89.47	92.38	94.01
CC(O[O])CCC	−24.27	101.42	35.67	43.68	50.83	56.86	66.27	73.19	83.84	89.23	92.15	93.97
CCC(O[O])(C)C	−28.62	95.14	37.05	45.39	52.49	58.35	67.37	73.99	84.22	89.44	92.28	94.02
CCC(O[O])CC	−24.08	98.29	35.99	44.49	51.94	58.09	67.43	74.16	84.45	89.63	92.30	94.17
[O]OC(C(C)(C)C)C	−32.49	100.55	41.13	51.34	60.27	67.69	78.99	87.10	99.25	105.20	108.53	110.41
[O]OC(C(C)C)(C)C	−34.13	99.91	43.48	53.64	62.07	68.95	79.47	87.16	98.99	105.00	108.33	110.31
[O]OCC(C(C)C)C	−26.78	106.32	42.27	51.91	60.41	67.49	78.42	86.41	98.66	104.91	108.15	110.14
[O]OCCC(C)(C)C	−28.22	103.04	40.81	50.75	59.76	67.32	78.83	87.02	99.22	105.22	108.55	110.38
CCC(CO[O])(C)C	−28.33	102.79	41.72	51.78	60.76	68.29	79.72	87.82	99.74	105.55	108.85	110.46
[O]OC(C(C)C)C(C)C	−36.18	106.91	48.76	61.92	72.41	80.52	92.37	100.95	114.10	120.78	124.50	126.63
[O]OC(CC(C)C)(C)C	−39.24	107.15	49.67	61.51	71.72	80.10	92.65	101.53	114.75	121.37	124.72	126.98

Table 3 displays properties, corrected to 298 K with heat capacity functions, for C_2H_5, n-C_3H_7, i-C_3H_7, n-C_4H_9, s-C_4H_9, i-C_4H_9, t-C_4H_9. Bodi et al. [94] obtain dissociation energies with threshold photoelectron photoion coincidence (TPEPICO) spectroscopy. They derive 298 K heats of formation for C_1–C_3 alkyl radicals with the TPEPICO onsets and heats of formation from CBS-APNO calculations and B3LYP/6-311+G(d,p) internal rotation curves on top of isodesmic schemes. Table 3 compiles their properties and provides the Baulch et al. recommended values based on experimental values, when available, and ab initio and group additivity methods [95].

Our **STAR-1D** procedure has computed heats of formation for each radical, bolded in Table 3, within all experimental uncertainties with the exception of i-C_3H_7. For i-C_3H_7, the **STAR-1D** heat of formation is well within the uncertainty from Seetula et al. [8] and is within the combination of its own and experimental uncertainty from Bodi et al. [94] Baulch et al., however, recommended the central value of Seakins et al. [7], which is a 0.69 kcal mol^{-1} higher value. Our success across the remaining alkyl radicals, and our uncertainty analysis, suggests that the 21.51 kcal mol^{-1} value for i-C_3H_7 is an over-estimate. The same species also experiences the greatest entropy difference, where the **STAR-1D** entropy is 0.7 cal mol^{-1} K^{-1} outside of the experimental uncertainty from Seetula et al. [8]. It is, however, within the Seakins et al. [7] report. The **STAR-1D** entropies in this comparison are otherwise all within the combination of experimental uncertainty and the uncertainty assigned to the computational approach.

Equilibrium constants, K_{eq}, provide a more direct comparison to experimental measurement. We calculate K_{eq} $\mathbf{\dot{R} + O_2 \rightleftharpoons R\dot{O}_2}$ from the Gibbs energies of alkyl and alkylperoxy radicals, or their partition functions, which are both available from the **STAR-1D** analysis. Slagle and co-workers studied this equilibrium for several alkyl radicals through photolysis of RX, monitoring relaxation in the presence of O_2 with PI-MS [9–11]. Figure 14 displays the **STAR-1D** equilibrium constant, K_{eq}, in contrast to the $K_{p,old}$ from these works and a re-formulated $K_{p,new}$, from Knyazev and Slagle [12], which accounts for further reaction of the $\mathbf{R\dot{O}_2}$ adduct. For the largest of the species, t-C_4H_9, the **STAR-1D** computed K_{eq} is within reported experimental uncertainties for the entire temperature range. While the i-C_3H_7 K_{eq} is also within experimental uncertainties at low

Table 6
STAR-1D heat of formation (ΔH_f) in kcal mol^{-1} and entropy (S) and heat capacities (C_p) in cal mol^{-1} K^{-1} for hydroperoxyalkyl radicals. Temperatures are in Kelvin.

SMILES	ΔH_f	S	C_p									
	298	298	300	400	500	600	800	1000	1500	2000	2500	3000
ȮOOH												
[CH$_2$]COO	12.62	78.69	20.67	23.89	26.80	29.25	33.06	35.88	40.33	42.66	43.95	44.73
[CH$_2$]CCOO	6.32	86.32	27.84	33.02	37.20	40.53	45.57	49.29	55.18	58.26	60.00	60.99
OOC([CH$_2$])C	3.61	86.67	27.19	31.84	35.96	39.41	44.73	48.66	54.82	58.02	59.81	60.83
C[CH]COO	4.22	89.73	25.17	29.89	34.18	37.91	43.65	47.93	54.51	57.77	59.75	60.82
[CH$_2$]CCCOO	1.26	97.06	32.16	38.68	44.55	49.48	56.50	61.73	69.64	73.67	75.88	77.18
[CH$_2$]C(OO)CC	−0.95	95.09	34.00	40.05	45.30	49.68	56.45	61.47	69.34	73.42	75.62	76.96
C[CH]CCOO	−1.20	97.11	32.70	38.76	44.19	48.78	55.92	61.18	69.31	73.46	75.79	77.08
CC[CH]COO	0.26	97.44	32.51	38.37	43.72	48.27	55.42	60.75	68.96	73.23	75.48	77.01
OOC([CH$_2$])(C)C	−5.52	90.78	34.02	40.27	45.63	50.03	56.75	61.68	69.42	73.45	75.70	77.04
CC(OO)[CH]C	−4.45	95.83	32.34	38.21	43.54	48.08	55.21	60.52	68.81	73.06	75.46	76.84
CC(OO)C[CH$_2$]	−2.14	95.21	32.94	39.38	45.03	49.74	56.57	61.67	69.50	73.54	75.78	77.09
OOC[C](C)C	−5.24	95.19	29.07	35.58	41.45	46.43	54.17	59.85	68.52	72.97	75.39	76.79
OOCC([CH2])C	0.00	96.48	31.50	37.90	43.65	48.55	55.82	61.20	69.37	73.50	75.77	77.10
[CH$_2$]C(CC)COO	−4.58	105.05	38.99	46.69	53.36	58.94	67.56	73.94	83.87	88.89	91.60	93.26
[CH$_2$]C(OO)CCC	−5.83	103.77	40.13	47.75	54.34	59.82	68.27	74.47	84.10	89.02	91.71	93.32
[CH$_2$]CC(OO)(C)C	−11.80	98.78	40.45	48.34	55.00	60.43	68.70	74.73	84.14	89.01	91.74	93.30
[CH$_2$]CCCCOO	−3.54	106.86	38.21	45.86	52.82	58.78	67.54	74.10	84.05	89.06	91.79	93.38
C[C](CC)COO	−8.98	108.13	36.24	43.58	50.50	56.41	65.64	72.49	83.02	88.40	91.30	92.87
C[CH]CCCOO	−6.45	108.99	36.36	44.00	51.14	57.33	66.45	73.29	83.59	88.76	91.57	93.21
CC([CH]C)COO	−7.50	105.15	38.65	45.73	52.18	57.79	66.44	72.99	83.17	88.40	91.28	92.99
CC(C[CH$_2$])COO	−5.41	105.88	39.27	46.57	52.97	58.46	66.98	73.39	83.40	88.54	91.38	93.05
CC[CH]CCOO	−6.31	108.68	36.24	43.81	51.00	57.27	66.43	73.27	83.55	88.73	91.55	93.20
CCC[CH]COO	−5.15	105.03	42.72	49.86	55.83	60.84	68.75	74.72	84.14	88.95	91.68	93.17
OOC[CH]C(C)C	−6.03	104.84	38.78	45.90	52.45	58.03	66.79	73.27	83.33	88.67	91.31	93.16
C[CH]C(OO)(C)C	−13.64	101.21	39.10	46.52	53.12	58.68	67.29	73.66	83.53	88.55	91.38	93.02
C[CH]C(OO)CC	−9.36	105.03	38.30	45.58	52.22	57.87	66.71	73.20	83.35	88.49	91.44	93.06
CC(OO)[CH]CC	−9.53	104.79	37.53	45.20	52.01	57.77	66.73	73.30	83.52	88.83	91.48	93.25
CC(OO)C[CH]C	−9.94	103.27	38.42	46.41	53.34	59.05	67.74	74.07	83.85	88.85	91.64	93.21
CC(OO)CC[CH$_2$]	−7.04	105.88	39.00	46.39	52.92	58.52	67.18	73.62	83.58	88.67	91.47	93.12
CCC(OO)([CH$_2$])C	−10.12	99.65	40.50	48.68	55.49	60.96	69.07	74.95	84.05	88.96	91.61	93.25
CCC(OO)C[CH$_2$]	−7.15	103.27	40.92	48.66	54.99	60.17	68.25	74.32	83.94	88.90	91.65	93.24
OOC([C](C)C)C	−13.78	102.74	37.25	44.85	51.75	57.45	66.48	73.01	83.22	88.46	91.27	93.09
OOC(C([CH$_2$])C)C	−8.20	101.15	39.21	47.36	54.24	59.85	68.28	74.42	83.97	88.94	91.72	93.24
OOC(C(C)C)[CH$_2$]	−7.32	100.47	40.42	48.11	54.61	59.97	68.27	74.42	83.99	88.94	91.66	93.30
OOCC([CH$_2$])(C)C	−7.19	101.83	36.86	44.85	52.06	58.20	67.23	73.87	83.88	88.93	91.69	93.30
OOCC[C](C)C	−9.85	103.85	38.90	45.63	51.94	57.45	66.30	72.98	83.29	88.52	91.39	93.14
OOCCC([CH$_2$])C	−4.86	103.78	38.68	46.56	53.46	59.26	67.85	74.22	83.97	88.94	91.67	93.27
[CH$_2$]CC(COO)(C)C	−12.39	108.80	44.19	53.48	61.90	69.11	79.69	87.41	98.94	104.71	107.84	109.66
C[CH]C(COO)(C)C	-14.42	112.49	42.66	51.49	59.87	67.22	78.12	86.16	98.19	104.20	107.48	109.39
CCC(COO)([CH$_2$])C	−11.20	112.02	43.93	53.09	61.31	68.33	78.74	86.44	98.17	104.14	107.41	109.34
OOC([C](C)C)C)(C)C	−21.80	106.52	43.39	52.54	60.75	67.66	78.32	86.06	97.90	103.94	107.30	109.20
OOC(C([CH$_2$])(C)C)C	−14.26	108.52	44.02	53.43	61.68	68.66	79.08	86.76	98.44	104.34	107.57	109.45
OOC(C(C)C)C)[CH$_2$]	−14.86	104.10	45.16	54.91	63.19	69.96	80.26	87.71	99.06	104.72	107.87	109.70
OOC(C(C)[CH$_2$])(C)C	−17.14	105.36	45.24	55.70	64.33	71.13	81.07	88.11	98.93	104.52	107.67	109.50
OOC(C(C)C)([CH$_2$])C	−15.87	105.20	46.39	56.41	64.65	71.19	80.90	87.86	98.76	104.41	107.59	109.47
OOC[C](C(C)C)C	−14.82	113.85	42.70	51.67	59.87	66.87	77.57	85.47	97.58	103.70	107.15	109.32
OOC[CH]C(C)(C)C	−13.81	106.44	45.13	54.23	62.30	69.29	79.88	87.52	98.95	104.68	107.87	109.73
OOCC([C](C)C)C	−15.78	114.85	40.79	49.47	57.81	65.17	76.20	84.49	97.06	103.43	106.92	108.97
OOCC(C([CH$_2$])C)C	−10.69	110.48	45.76	55.12	63.07	69.65	79.36	86.73	98.21	104.14	107.40	109.33
OOCC(C(C)C)[CH$_2$]	−10.83	109.25	45.06	54.59	62.76	69.53	79.43	86.86	98.33	104.22	107.47	109.38
OOCCC(C)(C)[CH$_2$]	−11.55	110.96	43.20	52.77	61.28	68.47	78.95	86.66	98.33	104.25	107.49	109.39
OOC([C](C)C)C(C)C	−25.44	112.40	50.16	61.09	70.96	79.26	91.84	100.81	113.95	120.41	123.91	126.01

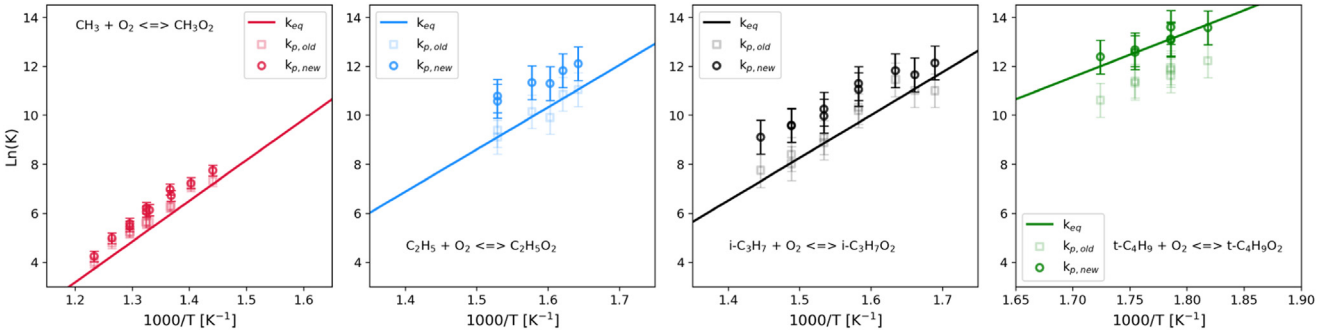

Fig. 14. Equilibrium constants, K, for $\dot{\mathbf{R}} + \mathbf{O}_2 \rightleftharpoons \mathbf{R}\dot{\mathbf{O}}_2$ where $\dot{\mathbf{R}}$ =CH_3, C_2H_5, i-C_3H_7, and t-C_4H_9. K_{eq} is computed with **STAR-1D** and shown as a solid line. $K_{p,old}$, the translucent circles, is from experiment, and $K_{p,new}$, the opaque circles, is reformulated equilibrium constants from experiment.

Table 7
STAR-1D heat of formation (ΔH_f) in kcal mol^{-1} and entropy (S) and heat capacities(C_p)in cal mol^{-1} K^{-1} for large species, which use CCSD(T)-F12/cc-pVDZ-F12 based CBH-ANL energies. Temperatures are in Kelvin.

SMILES	ΔH_f	S	C_p									
	298	298	300	400	500	600	800	1000	1500	2000	2500	3000
RH												
CC(CC(C)(C)C)(C)C	−57.83	101.00	50.36	65.22	78.78	90.34	108.12	120.68	138.78	147.39	151.95	154.56
RO_2H												
OOC(C(C)C)C(C)C	−67.25	109.29	50.45	63.85	74.64	83.07	95.55	104.58	118.46	125.48	129.27	131.59
OOC(CC(C)C)(C)C	−70.39	113.07	50.04	61.49	71.99	80.96	93.88	103.36	117.61	124.83	128.79	131.12
OOCC(CC(C)C)C	−65.84	114.80	51.22	63.70	74.09	82.51	95.18	104.41	118.28	125.31	129.18	131.55
OOC(C(C)(C)C)C(C)C	−72.11	118.22	56.10	68.57	79.93	89.76	104.63	115.62	132.20	140.44	144.90	147.48
OOC(CC(C)(C)C)(C)C	−75.74	113.51	55.77	70.04	82.58	92.86	108.03	118.47	133.73	141.29	145.45	147.87
OOCC(CC(C)(C)C)C	−72.73	113.82	55.35	70.98	84.54	95.37	110.72	120.92	135.49	142.48	146.31	148.59
OOCC(CC(C)C)(C)C	−71.15	118.83	56.08	69.84	81.87	91.84	106.97	117.76	133.81	141.57	145.66	148.16
$R\dot{O}_2$												
[O]OCC(CC(C)C)C	−33.06	112.92	48.63	60.59	70.80	79.13	91.71	100.68	114.14	121.01	124.57	126.78
[O]OC(C(C)(C)C)C(C)C	−40.45	116.14	52.08	65.62	77.47	87.23	101.93	112.41	128.07	135.93	140.29	142.69
[O]OC(CC(C)(C)C)(C)C	−44.04	111.32	53.59	67.31	79.53	89.64	104.65	114.94	129.84	137.09	140.97	143.22
[O]OCC(CC(C)(C)C)C	−39.12	116.77	53.78	67.24	79.16	89.02	103.78	114.15	129.35	136.68	140.91	143.28
[O]OCC(CC(C)C)(C)C	−38.06	116.98	53.08	66.50	78.60	88.67	103.77	114.30	129.69	137.05	141.00	143.44
ȮOOH												
OOC([CH]C(C)C)(C)C	−24.55	116.78	51.58	62.86	72.34	80.01	91.52	99.88	112.84	119.56	123.21	125.37
OOC(C([CH_2])C)C(C)C	−17.76	114.83	53.42	64.26	73.20	80.54	91.72	100.05	113.03	119.70	123.39	125.56
OOC(C[C](C)C)(C)C	−27.73	113.57	50.97	61.55	70.75	78.44	90.36	99.12	112.61	119.54	123.18	125.57
OOC(CC([CH_2])C)(C)C	−21.07	117.70	50.28	61.31	71.03	79.20	91.07	99.79	113.01	119.72	123.41	125.58
OOC(CC(C)C)([CH_2])C	−19.87	117.00	53.81	63.97	72.81	80.29	91.63	99.99	112.96	119.64	123.33	125.51
OOC[C](CC(C)C)C	−21.05	120.01	49.63	60.34	69.93	77.93	90.19	99.12	112.60	119.55	123.29	125.41
OOCC([CH]C(C)C)C	−19.20	124.13	49.63	59.84	69.00	76.88	88.88	97.91	111.85	118.98	122.90	125.21
OOCC(C[C](C)C)C	−22.07	122.73	47.71	58.18	67.78	76.08	88.54	97.81	111.91	119.05	122.96	125.25
OOCC(CC([CH_2])C)C	−16.44	118.69	51.62	63.04	72.50	80.15	91.82	100.33	113.41	120.06	123.67	125.89
OOCC(CC(C)C)[CH_2]	−16.25	118.54	51.18	62.66	72.38	80.27	92.17	100.68	113.64	120.18	123.85	125.92
OOC([CH]C(C)(C)C)(C)C	−29.52	118.60	57.63	70.58	81.40	90.16	103.39	112.91	127.49	135.02	139.11	141.71
OOC(C([CH_2])(C)C)C(C)C	−22.17	123.52	57.70	69.62	79.94	88.67	101.98	111.86	127.09	134.85	139.11	141.62
OOC(C(C)(C)C)[C](C)C	−32.31	117.81	53.53	66.91	79.00	89.08	104.08	114.36	129.00	136.12	139.87	142.27
OOC(C(C)(C)C)C(C)[CH_2]	−22.64	121.83	54.47	67.26	78.62	88.20	102.15	112.38	127.68	135.33	139.49	141.90
OOC(CC([CH_2])(C)C)(C)C	−26.22	117.83	59.39	72.14	82.79	91.60	104.81	114.27	128.63	135.84	139.80	142.11
OOC(CC(C)(C)C)([CH_2])C	−25.60	121.17	55.68	69.00	80.67	90.40	104.33	114.18	128.67	135.87	139.82	142.11
OOC[C](CC(C)(C)C)C	−28.35	121.68	54.81	67.76	79.34	88.94	103.34	113.40	128.31	135.71	139.74	142.13
OOCC([CH]C(C)(C)C)C	−26.54	121.22	56.80	70.55	82.27	91.66	105.44	114.99	129.14	136.16	139.96	142.35
OOCC([CH]C(C)C)(C)C	−25.28	124.90	55.62	67.60	78.99	88.91	103.27	113.52	128.46	135.82	139.81	142.13
OOCC(C[C](C)C)(C)C	−29.40	122.47	55.76	67.96	78.83	88.12	102.63	113.10	128.61	136.16	140.10	142.44
OOCC(CC([CH_2])(C)C)C	−22.33	123.58	57.54	70.59	81.64	90.68	103.65	113.21	127.80	135.26	139.38	141.80
OOCC(CC([CH_2])C)(C)C	−22.34	120.98	58.41	71.41	82.44	91.49	105.19	114.97	129.56	136.77	140.52	142.69
OOCC(CC(C)(C)C)[CH_2]	−23.28	119.22	56.19	70.59	82.68	92.24	106.04	115.58	129.67	136.65	140.43	142.72
OOCC(CC(C)C)([CH_2])C	−21.19	126.79	56.68	68.50	79.34	88.66	102.37	112.46	127.62	135.25	139.41	141.84

temperatures, it has the highest discrepancy from $K_{p,new}$ at high temperatures. At 675 K, for example, $K_{p,new} - K_{eq} = \exp(0.98) = 2.7$ which corresponds to a $\Delta G = 3.6$ kcal mol^{-1}. The degree of agreement otherwise on these plots demonstrates the success of the **STAR-1D** for computing not just enthalpies, entropies, and heat capacities, but also for equilibrium constants.

3.9. Presentation of data

The final thermodynamic properties produced with the **STAR-1D** method establish a substantial and systematically-derived dataset. Heats of formation at 298 K, entropies at 298 K, and heat capacities at selected temperatures in the range 300–3000 K are presented for **RH** and **Ṙ** species in Table 4, for **RO_2H** and **$R\dot{O}_2$** species in Table 5, and for **ȮOOH** radicals in Table 6. Table 7 contains the same properties for large species, for which the CBH-ANL 0 K heat of formation are based on CCSD(T)-F12/cc-pVDZ-F12 calculations. Gibbs energies for selected temperatures in the range 300 and 3000 K are provided in Tables S4.6–9. The MESS input files, in Section S6.1–2, present B2PLYP-D3/cc-pVTZ geometries, scaled B2PLYP-D3/cc-pVTZ frequencies, where rotational, translational, and torsional modes are projected from the Hessian, and 1D ωB97X-D/cc-pVTZ torsional profiles. Section S5.4 provides unscaled B2PLYP-D3/cc-pVTZ harmonic frequencies and geometries for all reference conformers, as well as the 461 conformers for species with seven heavy atoms or fewer. NASA polynomials, given in Section S7.1–3, will facilitate direct application of the data produced with the **STAR-1D** method in future simulations.

4. Conclusions

Novel to **STAR-1D** are two physically based scale factors. The first scales a torsional profile to approximate that obtained using a higher-level of theory while capturing effects from torsional coupling. By comparing properties based on scaled ωB97X-D/cc-pVTZ 1D torsional profiles to those calculated with full multi-dimensional partition functions for five species, we evaluate that ΔG(800 K) has no more than 0.8 kcal mol^{-1} uncertainty due to remaining multi-dimensional effects. Within the 1DHR model, we find low sensitivity of thermochemical properties to electronic structure method used during the torsional scans, even without the scale factor. Specifically, we predict the ωB97X-D/cc-pVTZ method produces no more than 0.3 cal mol^{-1} K^{-1} difference in entropies than those from high-level methods for the most sensitive species. This torsional scaling reduced the interquartile range of error in heat capacities for C_3–C_7 *n*-alkanes by nearly a factor of two when compared to experimental values at 600–1000 K.

The second scaling factor introduced in this work is a frequency-dependent harmonic frequency scale factor to approximate B2PLYP-D3/cc-pVTZ anharmonic frequencies and optimized

for contribution to partition functions and resulting in a 2σ of 1.4% for each mode. This easily applied frequency scale factor reduced mean error from experimental heat capacities by more than a factor of two in the temperature range 300–1500 K.

The RRHO + 1DHR partition functions additionally introduce significant sensitivity to conformer selection. The sensitivity is heightened in the presence of hydrogen bonding. This work carries out a detailed conformer analysis on 461 conformers for alkane oxidation species with fewer than eight heavy atoms to evaluate the applicability of four assumptions that the **STAR-1D** procedure makes in its conformer selection. The analysis concludes that a sufficient number of geometries are considered for each species, by optimizing a number of geometries equal to the lesser of 100 and $6 + 2(3^n)$ where n is the number of non-methyl torsional coordinates. For 2% of non-**$\dot{Q}$OOH** species, the electronic minimum energy conformer on the ωB97X-D/6-31G* PES differed from that on the B2PLYP-D3/cc-pVTZ PES by more than 0.33 kcal mol^{-1}. We recommend that, in future work, any rotamers within this energy threshold are re-optimized at B2PLYP-D3/cc-pVTZ and to select the resulting minimum energy conformer on the B2PLYP-D3/cc-pVTZ PES. Common to **$\dot{Q}$OOH** species, we find that, in the presence of hydrogen bonds, the ZPVE can alter which conformer is the 0 K minimum energy structure. Moreover, the rigidity that hydrogen bonding adds to a structure reduces the entropy, causing hydrogen bonded structures to have a higher Gibbs energy at temperatures $>$ 0 K. Because of this, we re-evaluate the thermochemistry of 31 species to select non-hydrogen bonded structures, which on average results in Gibbs energies that are 4 kcal mol^{-1} lower than those from the original hydrogen bonded conformers at 1000 K.

The upper limit to the 2σ uncertainties in the **STAR-1D** protocol for these species is estimated at 0.6–1.2 kcal mol^{-1} for ΔG(800 K). The uncertainties are expected to increase in order **RH** $<$ **RO$_2$H** $<$ **R$\dot{O}_2$** $<$ **$\dot{R}$** $<$ **$\dot{Q}$OOH**. If trying to do uncertainty weighted optimization of a final kinetic model, like von Lehm [3], it would be appropriate to apply this uncertainty spectrum to the species. We report thermochemical parameters for the reference conformers of 195 species, for 16 species that are used for the CBH-ANL energies, and for an additional lowest-energy non-hydrogen bonded conformer for 31 species. We additionally compute **STAR-1D** ΔH_f(0 K) for 461 conformers for the alkane oxidation species with seven or fewer heavy atoms. This dataset will facilitate isolation of very specific group contributions for development of group additivity values and machine learning descriptors. The data will also find utility in direct insertion into low-temperature oxidation mechanisms.

Declaration of Competing Interest

The authors declare that they have no known competing financial interests or personal relationships that could have appeared to influence the work reported in this paper.

Acknowledgments

Sarah N. Elliott is supported by the Exascale Computing Project (ECP), Project no.: 17-SC-20-SC, a collaborative effort of two U.S. Department of Energy (DOE) organizations, the Office of Science and the National Nuclear Security Administration, responsible for the planning and preparation of a capable exascale ecosystem including software, applications, hardware, advanced system engineering, and early test bed platforms to support the nation's exascale computing imperative. Part of this material is based on work at Argonne supported by the U.S. Department of Energy, Office of Basic Energy Sciences, Division of Chemical Sciences, Geosciences, and Biosciences, under Contract no. DE-AC02-06CH11357 as part of the Gas Phase Chemical Physics program. The authors at NUI Galway acknowledge funding from Science Foundation Ireland via project numbers 15/IA/3177 and the Irish Centre for High-End Computing (ICHEC).

Supplementary material

Supplementary material associated with this article can be found, in the online version, at doi:10.1016/j.combustflame.2022.112487

References

[1] T. Lu, C.K. Law, Toward accommodating realistic fuel chemistry in large-scale computations, Prog. Energy Combust. Sci. 35 (2) (2009) 192–215, doi:10.1016/j.pecs.2008.10.002.
[2] K.J. Hughes, J.F. Griffiths, M. Fairweather, A.S. Tomlin, Evaluation of models for the low temperature combustion of alkanes through interpretation of pressure-temperature ignition diagrams, Phys. Chem. Chem. Phys. 8 (2006) 3197–3210, doi:10.1039/b605379c.
[3] F. vom Lehn, L. Cai, H. Pitsch, Sensitivity analysis, uncertainty quantification, and optimization for thermochemical properties in chemical kinetic combustion models, Proc. Combust. Inst. 37 (1) (2019) 771–779, doi:10.1016/j.proci.2018.06.188. https://www.sciencedirect.com/science/article/pii/S1540748918303742
[4] F. vom Lehn, L. Cai, H. Pitsch, Investigating the impacts of thermochemical group additivity values on kinetic model predictions through sensitivity and uncertainty analyses, Combust. Flame 213 (2020) 394–408, doi:10.1016/j.combustflame.2019.12.011.
[5] A.S. Hansen, T. Bhagde, K.B. Moore, D.R. Moberg, A.W. Jasper, Y. Georgievskii, M.F. Vansco, S.J. Klippenstein, M.I. Lester, Watching a hydroperoxyalkyl radical ($\dot{Q}$OOH) dissociate, Science 373 (6555) (2021) 679–682, doi:10.1126/science.abj0412.
[6] J.A. Seetula, J.J. Russell, D. Gutman, Kinetics and thermochemistry of the reactions of alkyl radicals (methyl, ethyl, isopropyl, sec-butyl, tert-butyl) with hydrogen iodide: a reconciliation of the alkyl radical heats of formation, J. Am. Chem. Soc. 112 (4) (1990) 1347–1353, doi:10.1021/ja00160a009.
[7] P.W. Seakins, M.J. Pilling, J.T. Niiranen, D. Gutman, L.N. Krasnoperov, Kinetics and thermochemistry of R + HBr = RH + Br reactions: determinations of the heat of formation of ethyl, isopropyl, sec-butyl and tert-butyl radicals, J. Phys. Chem. 96 (24) (1992) 9847–9855, doi:10.1021/j100203a050.
[8] J.A. Seetula, I.R. Slagle, Kinetics and thermochemistry of the R + HBr = RH + Br (r = n-C_3H_7, iso-C_3H_7, n-C_4H_9, iso-C_4H_9, sec-C_4H_9 or tert-C_4H_9) equilibrium, J. Chem. Soc., Faraday Trans. 93 (1997) 1709–1719, doi:10.1039/A608224F.
[9] I.R. Slagle, D. Gutman, Kinetics of polyatomic free radicals produced by laser photolysis. 5. Study of the equilibrium $CH_3 + O_2 = CH_3O_2$ between 421 and 538 K, J. Am. Chem. Soc. 107 (19) (1985) 5342–5347, doi:10.1039/A608224F.
[10] I.R. Slagle, E. Ratajczak, D. Gutman, Study of the thermochemistry of the $C_2H_5 + O_2 = C_2H_5O_2$ and t-$C_4H_9 + O_2$ = t-$C_4H_9O_2$ reactions and of the trend in the alkylperoxy bond strengths, J. Phys. Chem. 90 (3) (1986) 402–407, doi:10.1021/j100275a010.
[11] I.R. Slagle, E. Ratajczak, M.C. Heaven, D. Gutman, A.F. Wagner, Kinetics of polyatomic free radicals produced by laser photolysis. 4. Study of the equilibrium iso-$C_3H_7 + O_2$ = iso-$C_3H_7O_2$ between 592 and 692 K, J. Am. Chem. Soc. 107 (7) (1985) 1838–1845, doi:10.1021/ja00293a006.
[12] V.D. Knyazev, I.R. Slagle, Thermochemistry of the R-O_2 bond in alkyl and chloroalkyl peroxy radicals, J. Phys. Chem. A 102 (10) (1998) 1770–1778, doi:10.1021/jp9726091.
[13] S.W. Benson, J.H. Buss, Additivity rules for the estimation of molecular properties. Thermodynamic properties, J. Chem. Phys. 29 (3) (1958) 546–572, doi:10.1063/1.1744539.
[14] S.W. Benson, et al., Thermochemical Kinetics, John Wiley and Sons, New York, 1976.
[15] N. Cohen, S.W. Benson, Estimation of heats of formation of organic compounds by additivity methods, Chem. Rev. 93 (7) (1993) 2419–2438, doi:10.1021/cr00023a005.
[16] N. Cohen, Revised group additivity values for enthalpies of formation (at 298 K) of carbon-hydrogen and carbon-hydrogen-oxygen compounds, J. Phys. Chem. Ref. Data 25 (6) (1996) 1411–1481, doi:10.1063/1.555988.
[17] J.L. Holmes, C. Aubry, Group additivity values for estimating the enthalpy of formation of organic compounds: an update and reappraisal. 2. C, H, N, O, S, and halogens, J. Phys. Chem. A 116 (26) (2012) 7196–7209, doi:10.1021/jp303780m.
[18] S.P. Verevkin, Thermochemistry of nitro compounds. experimental standard enthalpies of formation and improved group-additivity values, Thermochim. Acta 307 (1) (1997) 17–25, doi:10.1016/S0040-6031(97)00359-6.
[19] S.P. Verevkin, V.N. Emel'yanenko, V. Diky, C.D. Muzny, R.D. Chirico, M. Frenkel, New group-contribution approach to thermochemical properties of organic compounds: hydrocarbons and oxygen-containing compounds, J. Phys. Chem. Ref. Data 42 (3) (2013) 033102, doi:10.1063/1.4815957.
[20] T.H. Lay, J.W. Bozzelli, A.M. Dean, E.R. Ritter, Hydrogen atom bond increments for calculation of thermodynamic properties of hydrocarbon radical species, J. Phys. Chem. 99 (39) (1995) 14514–14527, doi:10.1021/j100039a045.

[21] R. Sumathi, W.H. Green, Thermodynamic properties of ketenes: group additivity values from quantum chemical calculations, J. Phys. Chem. A 106 (34) (2002) 7937–7949, doi:10.1021/jp021179y.

[22] R. Sumathi, W.H. Green, Missing thermochemical groups for large unsaturated hydrocarbons: contrasting predictions of G2 and CBS-Q, J. Phys. Chem. A 106 (46) (2002) 11141–11149, doi:10.1021/jp0215320.

[23] R. Sumathi, W.H. Green Jr., Oxygenate, oxyalkyl and alkoxycarbonyl thermochemistry and rates for hydrogen abstraction from oxygenates, Phys. Chem. Chem. Phys. 5 (2003) 3402–3417, doi:10.1039/B307050F.

[24] C.-C. Chen, J.W. Bozzelli, Structures, intramolecular rotation barriers, and thermochemical properties of methyl ethyl, methyl isopropyl, and methyl tert-butyl ethers and the corresponding radicals, J. Phys. Chem. A 107 (22) (2003) 4531–4546, doi:10.1021/jp022131n.

[25] M.K. Sabbe, F. De Vleeschouwer, M.-F. Reyniers, M. Waroquier, G.B. Marin, First principles based group additive values for the gas phase standard entropy and heat capacity of hydrocarbons and hydrocarbon radicals, J. Phys. Chem. A 112 (47) (2008) 12235–12251, doi:10.1021/jp807526n.

[26] P.D. Paraskevas, M.K. Sabbe, M.-F. Reyniers, N. Papayannakos, G.B. Marin, Group additive values for the gas-phase standard enthalpy of formation, entropy and heat capacity of oxygenates, Chem. Eur. J. 19 (48) (2013) 16431–16452, doi:10.1002/chem.201301381.

[27] S.S. Khan, X. Yu, J.R. Wade, R.D. Malmgren, L.J. Broadbelt, Thermochemistry of radicals and molecules relevant to atmospheric chemistry: determination of group additivity values using G3//B3LYP theory, J. Phys. Chem. A 113 (17) (2009) 5176–5194, doi:10.1021/jp809361y.

[28] S.M. Villano, L.K. Huynh, H.-H. Carstensen, A.M. Dean, High-pressure rate rules for alkyl + O_2 reactions. 1. The dissociation, concerted elimination, and isomerization channels of the alkyl peroxy radical, J. Phys. Chem. A 115 (46) (2011) 13425–13442, doi:10.1021/jp2079204.

[29] N. Sebbar, H. Bockhorn, J.W. Bozzelli, Structures, thermochemical properties (enthalpy, entropy and heat capacity), rotation barriers, and peroxide bond energies of vinyl, allyl, ethynyl and phenyl hydroperoxides, Phys. Chem. Chem. Phys. 4 (2002) 3691–3703, doi:10.1039/B111303H.

[30] N. Sebbar, J.W. Bozzelli, H. Bockhorn, Thermochemical properties, rotation barriers, bond energies, and group additivity for vinyl, phenyl, ethynyl, and allyl peroxides, J. Phys. Chem. A 108 (40) (2004) 8353–8366, doi:10.1021/jp031067m.

[31] C.F. Goldsmith, G.R. Magoon, W.H. Green, Database of small molecule thermochemistry for combustion, J. Phys. Chem. A 116 (36) (2012) 9033–9057, doi:10.1021/jp303819e.

[32] D.S. Farina, S.K. Sirumalla, E.J. Mazeau, R.H. West, Extensive high-accuracy thermochemistry and group additivity values for halocarbon combustion modeling, Ind. Eng. Chem. Res. 60 (43) (2021) 15492–15501, doi:10.1021/acs.iecr.1c03076.

[33] S.M. Burke, J.M. Simmie, H.J. Curran, Critical evaluation of thermochemical properties of C_1–C_4 species: updated group-contributions to estimate thermochemical properties, J. Phys. Chem. Ref. Data 44 (1) (2015) 013101, doi:10.1063/1.4902535.

[34] M. Keçeli, S.N. Elliott, Y.-P. Li, M.S. Johnson, C. Cavallotti, Y. Georgievskii, W.H. Green, M. Pelucchi, J.M. Wozniak, A.W. Jasper, et al., Automated computational thermochemistry for butane oxidation: a prelude to predictive automated combustion kinetics, Proc. Combust. Inst. 37 (1) (2019) 363–371, doi:10.1016/j.proci.2018.07.113.

[35] S.N. Elliott, K.B. Moore, A.V. Copan, M. Keçeli, C. Cavallotti, Y. Georgievskii, H.F. Schaefer, S.J. Klippenstein, Automated theoretical chemical kinetics: predicting the kinetics for the initial stages of pyrolysis, Proc. Combust. Inst. 38 (1) (2021) 375–384, doi:10.1016/j.proci.2020.06.019. https://www.sciencedirect.com/science/article/pii/S1540748920300456

[36] A.G. Dana, M. Johnson, J. Allen, S. Sharma, S. Raman, M. Liu, C. Gao, C. Grambow, M. Goldman, D. Ranasinghe, et al., Automated reaction kinetics and network exploration (arkane): a statistical mechanics, thermodynamics, transition state theory, and master equation software, ChemRxiv (2022).

[37] C. Cavallotti, M. Pelucchi, Y. Georgievskii, S.J. Klippenstein, Estoktp: electronic structure to temperature- and pressure-dependent rate constants-a code for automatically predicting the thermal kinetics of reactions, J. Chem. Theory Comput. 15 (2) (2019) 1122–1145, doi:10.1021/acs.J. Chem. Theory Comput. .8b00701.

[38] M.K. Ghosh, S.N. Elliott, K.P. Somers, S.J. Klippenstein, H.J. Curran, Group additivity values for the heat of formation of C_2–C_8 alkanes, alkyl hydroperoxides, and their radicals, 2022. Submitted.

[39] L. Zhu, J.W. Bozzelli, L.M. Kardos, Thermochemical properties, Δ_f H(298), S(298), and C_p(T), for n-butyl and n-pentyl hydroperoxides and the alkyl and peroxy radicals, transition states, and kinetics for intramolecular hydrogen shift reactions of the peroxy radicals, J. Phys. Chem. A 111 (2007) 6361–6377, doi:10.1021/jp070342s.

[40] R. Asatryan, J.W. Bozzelli, Chain branching and termination in the low-temperature combustion of n-alkanes: 2-pentyl radical + O_2, isomerization and association of the second O_2, J. Phys. Chem. A 114 (2010) 7693–7708, doi:10.1021/jp101159h.

[41] J.M. Hudzik, J.W. Bozzelli, Calculated entropies for n-heptane, 2-methylhexane, 2,3-dimethylpentane, and radicals from the loss of H atoms, Adv. Phys. Chem. 2013 (2013) 673065, doi:10.1155/2013/673065.

[42] I. Auzmendi-Murua, J.W. Bozzelli, Thermochemistry, reaction paths, and kinetics on the secondary isooctane radical reaction with $^3O_2$, Int. J. Chem. Kinet. 46 (2014) 71–103, doi:10.1002/kin.20825.

[43] J.M. Hudzik, J.W. Bozzelli, J.M. Simmie, Thermochemistry of C_7H_{16} to $C_{10}H_{22}$ alkane isomers: primary, secondary, and tertiary C–H bond dissociation energies and effects of branching, J. Phys. Chem. A 118 (2014) 9364–9379, doi:10.1021/jp503587b.

[44] S. Snitsiriwat, J.W. Bozzelli, Thermochemistry, reaction paths, and kinetics on the tert-isooctane radical reaction with O_2, J. Phys. Chem. A (118) (2014) 4631–4666, doi:10.1021/jp502702f.

[45] H. Wang, J.W. Bozzelli, Thermochemical properties (ΔH_f(298 K), S(298 K), C_p(T)) and bond dissociation energies for C1–C4 normal hydroperoxides and peroxy radicals, J. Chem. Eng. Data 61 (2016) 1836–1849, doi:10.1021/acs.jced.5b01035.

[46] P. Vansteenkiste, V. Van Speybroeck, G.B. Marin, M. Waroquier, Ab initio calculation of entropy and heat capacity of gas-phase n-alkanes using internal rotations, J. Phys. Chem. A 107 (17) (2003) 3139–3145, doi:10.1021/jp027132u.

[47] V. Van Speybroeck, D. Van Neck, M. Waroquier, Ab initio study of radical reactions: role of coupled internal rotations on the reaction kinetics (III), J. Phys. Chem. A 106 (38) (2002) 8945–8950, doi:10.1021/jp025836y.

[48] V. Van Speybroeck, P. Vansteenkiste, D. Van Neck, M. Waroquier, Why does the uncoupled hindered rotor model work well for the thermodynamics of n-alkanes? Chem. Phys. Lett. 402 (4–6) (2005) 479–484.

[49] B.M. Wong, W.H. Green, Effects of large-amplitude torsions on partition functions: beyond the conventional separability assumption, Mol. Phys. 103 (6–8) (2005) 1027–1034, doi:10.1080/00268970412331333627.

[50] S. Sharma, S. Raman, W.H. Green, Intramolecular hydrogen migration in alkylperoxy and hydroperoxyalkylperoxy radicals: accurate treatment of hindered rotors, J. Phys. Chem. A 114 (2010) 5689–5701, doi:10.1021/jp9098792.

[51] S.M. Villano, L.K. Huynh, H.-H. Carstensen, A.M. Dean, High-pressure rate rules for alkyl + O_2 reactions. 2. The isomerization, cyclic ether formation, and β–scission reactions of hydroperoxy alkyl radicals, J. Phys. Chem. A 116 (2012) 5068–5089, doi:10.1021/jp3023887.

[52] A. Miyoshi, Systematic computational study on the unimolecular reactions of alkylperoxy (RO_2), hydroperoxyalkyl (ȮOOH), and hydroperoxyalkylperoxy (O_2ȮOOH) radicals, J. Phys. Chem. A 107 (2011) 3301–3325, doi:10.1021/jp112152n.

[53] S.N. Elliott, M. Keceli, M.K. Gosh, K. Somers, H.J. Curran, S.J. Klippenstein, High accuracy heats of formation for alkane oxidation: From small to large via the CBH-ANL method, 2022. Submitted.

[54] R.O. Ramabhadran, K. Raghavachari, Theoretical thermochemistry for organic molecules: development of the generalized connectivity-based hierarchy, J. Chem. Theory Comput. 7 (7) (2011) 2094–2103, doi:10.1021/ct200279q.

[55] R.O. Ramabhadran, K. Raghavachari, Connectivity-based hierarchy for theoretical thermochemistry: assessment using wave function-based methods, J. Phys. Chem. A 116 (28) (2012) 7531–7537, doi:10.1021/jp301421a.

[56] A. Sengupta, K. Raghavachari, Prediction of accurate thermochemistry of medium and large sized radicals using connectivity-based hierarchy (CBH), J. Chem. Theory Comput. 10 (10) (2014) 4342–4350, doi:10.1021/ct500484f.

[57] S.J. Klippenstein, L.B. Harding, B. Ruscic, Ab initio computations and active thermochemical tables hand in hand: heats of formation of core combustion species, J. Phys. Chem. A 121 (35) (2017) 6580–6602, doi:10.1021/acs.J. Phys. Chem. A.7b05945.

[58] Y. Georgievskii, J.A. Miller, M.P. Burke, S.J. Klippenstein, Reformulation and solution of the master equation for multiple-well chemical reactions, J. Phys. Chem. A 117 (46) (2013) 12146–12154, doi:10.1021/jp4060704.

[59] B.J. McBride, Computer Program for Calculating and Fitting Thermodynamic Functions, vol.1271, National Aeronautics and Space Administration, Office of Management, 1992.

[60] J.-D. Chai, M. Head-Gordon, Long-range corrected hybrid density functionals with damped atom–atom dispersion corrections, Phys. Chem. Chem. Phys. 10 (44) (2008) 6615–6620, doi:10.1039/B810189B.

[61] S. Grimme, J. Antony, S. Ehrlich, H. Krieg, A consistent and accurate ab initio parametrization of density functional dispersion correction (DFT-D) for the 94 elements H-Pu, J. Chem. Phys. 132 (15) (2010) 154104, doi:10.1063/1.3382344.

[62] T.H. Dunning, Gaussian basis sets for use in correlated molecular calculations. I. The atoms boron through neon and hydrogen, J. Chem. Phys. 90 (2) (1989) 1007–1023, doi:10.1063/1.456153.

[63] G. Knizia, T.B. Adler, H.-J. Werner, Simplified CCSD(T)-F12 methods: theory and benchmarks, J. Chem. Phys. 130 (5) (2009) 054104, doi:10.1063/1.3054300.

[64] M.M. Francl, W.J. Pietro, W.J. Hehre, J.S. Binkley, M.S. Gordon, D.J. DeFrees, J.A. Pople, Self-consistent molecular orbital methods. XXIII. Apolarization-type basis set for second-row elements, J. Chem. Phys. 77 (7) (1982) 3654–3665, doi:10.1063/1.444267.

[65] A.W. Jasper, Z.B. Gruey, L.B. Harding, Y. Georgievskii, S.J. Klippenstein, A.F. Wagner, Anharmonic rovibrational partition functions for fluxional species at high temperatures via monte carlo phase space integrals, J. Phys. Chem. A 122 (6) (2018) 1727–1740, doi:10.1021/acs.J. Phys. Chem. A.7b11722.

[66] S.N. Elliott, High-level automated thermochemistry: building from small to large, Work presented at 5th Annual Flame Chemistry Workshop, Virtual, 2020.

[67] H.H. Nielsen, The vibration-rotation energies of polyatomic molecules, Phys. Rev. 60 (1941) 794–810, doi:10.1103/PhysRev.60.794. https://link.aps.org/doi/10.1103/PhysRev.60.794

[68] H. Akima, A new method of interpolation and smooth curve fitting based on local procedures, J. ACM 17 (4) (1970) 589–602.

[69] P. Virtanen, R. Gommers, T.E. Oliphant, M. Haberland, T. Reddy, D. Cournapeau, E. Burovski, P. Peterson, W. Weckesser, J. Bright, S.J. van der Walt, M. Brett, J. Wilson, K.J. Millman, N. Mayorov, A.R.J. Nelson, E. Jones, R. Kern, E. Larson, C.J. Carey, I. Polat, Y. Feng, E.W. Moore, J. VanderPlas, D. Laxalde, J. Perktold, R. Cimrman, I. Henriksen, E.A. Quintero, C.R. Harris, A.M. Archibald,

A.H. Ribeiro, F. Pedregosa, P. van Mulbregt, S. Contributors, SciPy 1.0: fundamental algorithms for scientific computing in Python, Nat. Methods 17 (2020) 261–272, doi:10.1038/s41592-019-0686-2.
[70] G. Tasi, F. Mizukami, I. Pálinkó, J. Csontos, W. Győrffy, P. Nair, K. Maeda, M. Toba, S.-i. Niwa, Y. Kiyozumi, et al., Enumeration of the conformers of unbranched aliphatic alkanes, J. Phys. Chem. A 102 (39) (1998) 7698–7703, doi:10.1021/jp981866i.
[71] G. Tasi, F. Mizukami, J. Csontos, W. Győrffy, I. Pálinkó, Quantum algebraic–combinatoric study of the conformational properties of *n*-alkanes. II, J. Math Chem. 27 (3) (2000) 191–199, doi:10.1023/A:1026472102742.
[72] S. Tsuzuki, L. Schafer, H. Goto, E.D. Jemmis, H. Hosoya, K. Siam, K. Tanabe, E. Osawa, Investigation of intramolecular interactions in *n*-alkanes. cooperative energy increments associated with GG and GTG[g= gauche, t= trans] sequences, J. Am. Chem. Soc. 113 (12) (1991) 4665–4671, doi:10.1021/ja00012a040.
[73] D. Gruzman, A. Karton, J.M.L. Martin, Performance of ab initio and density functional methods for conformational equilibria of C_nH_{2n+2} alkane isomers ($n = 4$–8), J. Phys. Chem. A 113 (43) (2009) 11974–11983, doi:10.1021/ja00012a040.
[74] J.J. Lutz, J.N. Byrd, J.A. Montgomery Jr., Benchmark comparison of dual-basis double-hybrid density functional theory and a neural-network-optimized method for intermolecular interactions, J. Mol. Spec. 376 (2021) 111406, doi:10.1016/j.jms.2020.111406.
[75] J. Csontos, B. Nagy, L. Gyevi-Nagy, M. Kállay, G. Tasi, Enthalpy differences of the *n*-pentane conformers, J. Chem. Theory Comput. 12 (6) (2016) 2679–2688, doi:10.1016/j.jms.2020.111406.
[76] J.A. Plumley, J.J. Dannenberg, A comparison of the behavior of functional/basis set combinations for hydrogen-bonding in the water dimer with emphasis on basis set superposition error, J. Comput. Chem. 32 (8) (2011) 1519–1527, doi:10.1002/jcc.21729.
[77] P.G. Jasien, W.J. Stevens, Ab initio study of the hydrogen bonding interactions of formamide with water and methanol, J. Chem. Phys. 84 (6) (1986) 3271–3277, doi:10.1063/1.450257.
[78] D.R. Lide, CRC Handbook of Chemistry and Physics, seventy fourth ed., CRC Press Inc., Boca Raton, Fl, 1995.
[79] D.R. Stull, E.F. Westrum, G.C. Sinke, The Chemical Thermodynamics of Organic Compounds, J. Wiley New York, 1969.
[80] P. Linstrom, W. Mallard, The NIST chemistry webBook: A chemical data resource on the internet (2001).
[81] D.W. Scott, Chemical Thermodynamic Properties of Hydrocarbons and Related Substances: Properties of the Alkane Hydrocarbons, C1 Through C10, in the Ideal Gas State from 0 to 1500 K, Technical Report, U.S. Dept of the Interior, Bureau of Mines, 1974.
[82] H.W. Woolley, Calcuation of thermodynamic functions for polyatomic molecules, J. Res. Natl. Bur. Stand. 56 (2) (1956) 105–110.
[83] V.P. Barber, A.S. Hansen, Y. Georgievskii, S.J. Klippenstein, M.I. Lester, Experimental and theoretical studies of the doubly substituted methyl-ethyl criegee intermediate: infrared action spectroscopy and unimolecular decay to OH radical products, J. Chem. Phys. 152 (9) (2020) 094301, doi:10.1063/5.0002422.
[84] D.F. DeTar, Theoretical ab initio calculation of entropy, heat capacity, and heat content, J. Phys. Chem. A 102 (26) (1998) 5128–5141, doi:10.1021/jp010321c.
[85] J.P. Guthrie, Use of DFT methods for the calculation of the entropy of gas phase organic molecules: an examination of the quality of results from a simple approach, J. Phys. Chem. A 105 (37) (2001) 8495–8499, doi:10.1021/jp010321c.
[86] P. Pracht, S. Grimme, Calculation of absolute molecular entropies and heat capacities made simple, Chem. Sci. 12 (19) (2021) 6551–6568, doi:10.1039/D1SC00621E.
[87] J. Zheng, T. Yu, E. Papajak, I.M. Alecu, S.L. Mielke, D.G. Truhlar, Practical methods for including torsional anharmonicity in thermochemical calculations on complex molecules: the internal-coordinate multi-structural approximation, Phys. Chem. Chem. Phys. 13 (23) (2011) 10885–10907, doi:10.1039/C0CP02644A.
[88] P. Vansteenkiste, V. Van Speybroeck, E. Pauwels, M. Waroquier, How should we calculate multi-dimensional potential energy surfaces for an accurate reproduction of partition functions? Chem. Phys. 314 (1–3) (2005) 109–117, doi:10.1016/j.chemphys.2005.01.029.
[89] P. Vansteenkiste, D. Van Neck, V. Van Speybroeck, M. Waroquier, An extended hindered-rotor model with incorporation of coriolis and vibrational-rotational coupling for calculating partition functions and derived quantities, J. Chem. Phys. 124 (4) (2006) 044314, doi:10.1063/1.2161218.
[90] L. Simón-Carballido, J.L. Bao, T.V. Alves, R. Meana-Pañeda, D.G. Truhlar, A. Fernández-Ramos, Anharmonicity of coupled torsions: the extended two-dimensional torsion method and its use to assess more approximate methods, J. Chem. Theory Comput. 13 (8) (2017) 3478–3492, doi:10.1021/acs.jctc.7b00451.
[91] A. Fernández-Ramos, Accurate treatment of two-dimensional non-separable hindered internal rotors, J. Chem. Phys. 138 (13) (2013) 134112, doi:10.1063/1.4798407.
[92] J. Wu, H. Ning, X. Xu, W. Ren, Accurate entropy calculation for large flexible hydrocarbons using a multi-structural 2-dimensional torsion method, Phys. Chem. Chem. Phys. 21 (19) (2019) 10003–10010, doi:10.1039/C9CP00191C.
[93] J.L. Bao, L. Xing, D.G. Truhlar, Dual-level method for estimating multistructural partition functions with torsional anharmonicity, J. Chem. Theory Comput. 13 (6) (2017) 2511–2522, doi:10.1021/acs.jctc.7b00232.
[94] A. Bodi, J.P. Kercher, C. Bond, P. Meteesatien, B. Sztray, T. Baer, Photoion photoelectron coincidence spectroscopy of primary amines RCH_2NH_2 (R = H, CH_3, C_2H_5, C_3H_7, i-C_3H_7): Alkylamine and alkyl radical heats of formation by isodesmic reaction networks, J. Phys. Chem. A 110 (50) (2006) 13425–13433, doi:10.1021/jp064739s.
[95] D.L. Baulch, C.T. Bowman, C.J. Cobos, R.A. Cox, T. Just, J.A. Kerr, M.J. Pilling, D. Stocker, J. Troe, W. Tsang, R.W. Walker, J. Warnatz, Evaluated kinetic data for combustion modeling: supplement II, J. Phys. Chem. Ref. Data 34 (3) (2005) 757–1397, doi:10.1063/1.1748524.